INTERNATIONAL JOURNAL FOR NUMERICAL METHODS IN FLUIDS
Int. J. Numer. Meth. Fluids 2002; **40**:735–774 (DOI: 10.1002/fld.374)

Evaluation of Smagorinsky-based subgrid-scale models in a finite-volume computation

Petri Majander[*,†,‡] and Timo Siikonen[§,¶]

Laboratory of Applied Thermodynamics, Helsinki University of Technology, P.O. Box 4400, Helsinki, Finland

SUMMARY

Smagorinsky-based models are assessed in a turbulent channel flow simulation at $Re_b = 2800$ and $Re_b = 12\,500$. The Navier–Stokes equations are solved with three different grid resolutions by using a co-located finite-volume method. Computations are repeated with Smagorinsky-based subgrid-scale models. A traditional Smagorinsky model is implemented with a van Driest damping function. A dynamic model assumes a similarity of the subgrid and the subtest Reynolds stresses and an explicit filtering operation is required. A top-hat test filter is implemented with a trapezoidal and a Simpson rule. At the low Reynolds number computation none of the tested models improves the results at any grid level compared to the calculations with no model. The effect of the subgrid-scale model is reduced as the grid is refined. The numerical implementation of the test filter influences on the result. At the higher Reynolds number the subgrid-scale models stabilize the computation. An analysis of an accurately resolved flow field reveals that the discretization error overwhelms the subgrid term at $Re_b = 2800$ in the most part of the computational domain. Copyright © 2002 John Wiley & Sons, Ltd.

KEY WORDS: large-eddy simulation; subgrid-scale model; channel flow; finite-volume method

1. INTRODUCTION

In large-eddy simulation, the flow is divided into two size-dependent parts. The large-scale motion is sensitive to the boundary conditions and it is solved from the governing equations, whereas the small-scale motion is modelled. Smagorinsky [1] derived an eddy viscosity subgrid-scale model based on a Boussinesq approximation. Deardorff [2] computed a fully turbulent channel flow by using the Smagorinsky model. In order to avoid the excessive damping, he lowered the Smagorinsky constant in the model to the value of 0.1 from 0.17,

*Correspondence to: P. Majander, Laboratory of Applied Thermodynamics, Helsinki University of Technology, P.O. Box 4400, Helsinki, Finland.
†E-mail: petri.majander@hut.fi
‡Research Scientist.
§Professor.
¶E-mail: timo.siikonen@hut.fi

Contract/grant sponsor: Academy of Finland
Contract/grant sponsor: CODE Program of the National Technology Agency TEKES

Received June 2001
Revised March 2002

which is obtained theoretically by assuming the inertial range dynamics. Moin and Kim [3] applied a van Driest damping function to reduce the near-wall viscosity even further. The Smagorinsky model is absolutely dissipative and it is based on resolved strains. With gradient flows, non-zero residual stresses are predicted even for laminar flows. Piomelli *et al.* [4] modified the length-scale by adding an intermittancy function to turn off the model during the early stages of transition. Germano *et al.* [5] introduced a model that computed the coefficient as the calculation progresses. The model introduces a coarser test filter, and the subgrid stresses and the subtest stresses are modelled with the Smagorinsky model. The model provides a mechanism for the backscattering of energy from the small eddies to the large ones and it can adjust to the local flow. In a channel flow, a proper asymptotic behaviour near the wall was obtained and a transition from laminar to turbulent compared well with finely resolved direct numerical simulation (DNS). No *ad hoc* damping functions were needed. Lilly [6] suggested solving the dynamic coefficient by using a least-square method. Piomelli [7] extended the Reynolds number up to 47 100 (based on the centre-line velocity) and obtained good results with modest grid sizes, although the computations were resolved to the wall. Most of the large-eddy simulations over the past years have been performed by using spectral methods, where the idea of filtering is realized ideally. Computations of flows in complex domains, frequent cases in engineering applications, are difficult to solve by employing the spectral methods, and are usually performed with finite-difference or finite-volume methods. Balaras *et al.* [8] studied high-Reynolds-number channel flows with dynamic model combined with a difference method. They applied approximate boundary conditions and were able to obtain good results with coarse grids. Najjar and Tafti [9] studied the discrete test filters at a low Reynolds number $Re_\tau = 180$. They found that a high-order test filter produced a lower turbulent viscosity than a top-hat test filter. This dynamic procedure also sensed dissipative upwind-biased scheme and adjusted the dynamic constant accordingly. However, in their conclusion they were not convinced that inclusion of the SGS model would always produce better results in finite-difference approximations. The reason for this is due to numerical errors rather than due to the model itself, they concluded. Najjar and Tafti [10] studied the effect of the grid resolution in the channel flow simulation at a higher Reynolds number, $Re_\tau = 1050$. The coarse grid simulation predicted too low wall stresses and the core velocities were too high. They concluded that a coarse grid could not capture the energy-producing near-wall structures. The application of the test filter in all the directions (i.e. also in the inhomogeneous direction) decreased the SGS stresses. Sagaut *et al.* [11] computed the channel flow with various self-adaptive SGS models combined with a finite-difference scheme at $Re_\tau = 180$ and $Re_\tau = 400$. A general trend was that the addition of the SGS models decreased the wall stress.

In this study, a fully turbulent channel flow at Reynolds numbers 2800 and 12 500 (based on the bulk velocity) is the test case in the study of large-eddy simulation with a co-located finite-volume technique. The results from simulations with the constant and the dynamic Smagorinsky SGS models are compared to a non-modelled simulation. The effect of the grid resolution on the results is studied with and without the SGS model. The discrete test filter is implemented according to the trapezoidal rule and Simpson rule in the dynamic model.

In the next section, the governing equations and the models are presented. In Section 3, the numerical methods and implementations are described. In Sections 4 and 5, the characteristics of the test cases are described and the results are discussed. In Section 6, an instantaneous flow field of a very fine grid simulation is analyzed in order to study the discretization error present in the large eddy simulations. The conclusions are drawn in Section 7.

2. GOVERNING EQUATIONS

Incompressible and isothermal Navier–Stokes equations are written in tensorial notations

$$\frac{\partial u_i}{\partial x_i} = 0 \tag{1}$$

$$\frac{\partial u_i}{\partial t} + \frac{\partial u_i u_j}{\partial x_j} = -\frac{1}{\rho}\frac{\partial p}{\partial x_i} + \nu \frac{\partial^2 u_i}{\partial x_j \partial x_j} \tag{2}$$

where i and $j = 1, 2$ and 3 correspond to x, y and z. A repetition of the index within the term stands for a summation convention, u_i is the velocity in the i-direction, p is the pressure, ρ is the density and ν is the kinematic viscosity μ/ρ. Equations for large-eddy simulation are derived by filtering the Navier–Stokes equations in space. The filtering operation is defined by

$$\bar{f}(\mathbf{r}, t) = \int_V G(|\mathbf{r} - \mathbf{r}'|)\, f(\mathbf{r}', t)\, \mathrm{d}\mathbf{r}' \tag{3}$$

where V is the volume of filtering and G is the filter function, which must satisfy the normalization condition

$$\int_V G(|\mathbf{r} - \mathbf{r}'|)\, \mathrm{d}\mathbf{r}' = 1 \tag{4}$$

The length of the filter Δ divides the length-scales are resolved large ones and subgrid-scale (SGS) ones. After applying the filtering operation we obtain from Equations (1) and (2)

$$\frac{\partial \bar{u}_i}{\partial x_i} = 0 \tag{5}$$

$$\frac{\partial \bar{u}_i}{\partial t} + \frac{\partial \bar{u}_i \bar{u}_j}{\partial x_j} = -\frac{1}{\rho}\frac{\partial \bar{p}}{\partial x_i} - \frac{\partial \tau_{i,j}}{\partial x_i} + \nu \frac{\partial^2 \bar{u}_i}{\partial x_j \partial x_j} \tag{6}$$

where the incompressible form of the SGS stresses is written as

$$\tau_{ij} = \overline{u_i u_j} - \bar{u}_i \bar{u}_j \tag{7}$$

SGS stresses interact between the resolved (grid) scales and the unresolved (subgrid) scales. Equations (5) and (6) are often produced implicitly by the discretization and no explicit filtering is usually carried out in solving them. A finite-volume or a finite-difference dicretization involves a top-hat filter, which is written in one dimension as

$$G(x - x') = \begin{cases} \dfrac{1}{\Delta}; & \text{if } |x - x'| \leqslant \dfrac{\Delta}{2}, \\ 0; & \text{otherwise} \end{cases} \tag{8}$$

In order to solve the large-eddy Equations (5) and (6), the SGS stresses (7) must be modelled. The SGS model removes the energy from resolved scales mimicking the dissipative scales that are solved inaccurately. Probably the most widely used SGS model is the Smagorinsky

model [1], which is an eddy viscosity model based on the Boussinesq approximation of the form

$$\tau_{ij} - \frac{\delta_{ij}}{3}\tau_{kk} = -2\nu_T \bar{S}_{ij} = -2C\Delta^2|\bar{S}|\bar{S}_{ij} \tag{9}$$

which relates subgrid-scale stresses τ_{ij} to the eddy viscosity ν_T and the resolved-scale strain rate tensor

$$S_{ij} = \frac{1}{2}\left(\frac{\partial u_i}{\partial x_j} + \frac{\partial u_j}{\partial x_i}\right). \tag{10}$$

Above, $|\bar{S}| = \sqrt{2\bar{S}_{ij}\bar{S}_{ij}}$ is the magnitude of the strain tensor, and the length scale Δ is computed as $(\Delta x_1 \Delta x_2 \Delta x_3)^{1/3}$, where Δx_i is the grid spacing in the i-direction. A value of 0.17 for the constant C_s can be justified on a theoretical basis; however, in a channel flow Deardorff found that a smaller value 0.1 is better [2]. Furthermore, in the vicinity of the walls, the eddy viscosity must be reduced. This is usually carried out with the van Driest damping function:

$$\nu_T = \left[C_s(1 - e^{-y^+/25})\Delta\right]^2 |\bar{S}| \tag{11}$$

Germano *et al*. [5] presented a dynamic SGS model, where model coefficients are calculated during the simulation. This is based on the application of two different filters. In addition to the grid filter G, a test filter $\hat{G}$ is applied. The test filter width $\hat{\Delta}$ is larger than the grid filter width Δ, usually $\hat{\Delta} = 2\Delta$. The grid filter and the test filter are applied to the momentum equations (2) to obtain the following equation:

$$\frac{\partial \hat{\bar{u}}_i}{\partial t} + \frac{\partial \hat{\bar{u}}_i \hat{\bar{u}}_j}{\partial x_j} = -\frac{1}{\rho}\frac{\partial \hat{\bar{p}}}{\partial x_i} - \frac{\partial T_{ij}}{\partial x_i} - \nu \frac{\partial^2 \hat{\bar{u}}_i}{\partial x_j \partial x_j} \tag{12}$$

where subset stresses are given by

$$T_{ij} = \widehat{\bar{u}_i \bar{u}_j} - \hat{\bar{u}}_i \hat{\bar{u}}_j. \tag{13}$$

The test filter is now applied to the grid-filtered equations (6)

$$\frac{\partial \hat{\bar{u}}_i}{\partial t} + \frac{\partial \hat{\bar{u}}_i \hat{\bar{u}}_j}{\partial x_j} = -\frac{1}{\rho}\frac{\partial \hat{\bar{p}}}{\partial x_i} - \frac{\partial \hat{\tau}_{ij}}{\partial x_i} - \frac{\partial \mathscr{L}_{ij}}{\partial x_i} + \nu \frac{\partial^2 \hat{\bar{u}}_i}{\partial x_j \partial x_j} \tag{14}$$

$$\mathscr{L}_{ij} = \widehat{\bar{u}_i \bar{u}_j} - \hat{\bar{u}}_i \hat{\bar{u}}_j \tag{15}$$

Using Equations (12) and (14), the expression for $\mathscr{L}_{ij}$ can be written as

$$\mathscr{L}_{ij} = T_{ij} - \hat{\tau}_{ij}. \tag{16}$$

Equation (13) represent the subtest-scale stresses whose length-scale is less than the subtest filter width $\hat{\Delta}$. Equation (16) represent then the resolved turbulent stresses by the scales between the grid filter width Δ and the subtest filter width $\hat{\Delta}$. Both τ_{ij} and T_{ij} are modelled

by the same functional form of the Smagorinsky model:

$$\tau_{ij} - \frac{\delta_{ij}}{3}\tau_{kk} = -2C\Delta^2|\bar{S}|\bar{S}_{ij} = -2C\beta_{ij} \tag{17}$$

$$T_{ij} - \frac{\delta_{ij}}{3}T_{kk} = -2C\hat{\Delta}^2|\hat{\bar{S}}|\hat{\bar{S}}_{ij} = -2C\alpha_{ij} \tag{18}$$

Substitution of stresses (17) and (18) into Equation (16) with the assumption of a slow variation of $C(C(x,y,z,t) \approx \hat{C}(x,y,z,t))$ gives

$$\mathscr{L}_{ij} - \frac{\delta_{ij}}{3}\mathscr{L}_{kk} = -2C\left(\hat{\Delta}^2|\hat{\bar{S}}|\hat{\bar{S}}_{ij} - \Delta^2\widehat{|\bar{S}|\bar{S}_{ij}}\right) \tag{19}$$

In order to solve the set of equations for C in Eq. (19), Lilly [6] proposed solving Eq. (19) in the least-square sense. The error

$$Q = \left(\mathscr{L}_{ij} - \frac{\delta_{ij}}{3}\mathscr{L}_{kk} - 2CM_{ij}\right)^2 \tag{20}$$

where

$$M_{ij} = \left(\hat{\Delta}^2|\hat{\bar{S}}|\hat{\bar{S}}_{ij} - \Delta^2\widehat{|\bar{S}|\bar{S}_{ij}}\right) \tag{21}$$

is minimized by requiring $\partial Q/\partial C = 0$, which gives

$$C(x,y,z,t) = -\frac{\mathscr{L}_{ij}M_{ij}}{2M_{ij}M_{ij}} \tag{22}$$

The numerator $\mathscr{L}_{ij}M_{ij}$ can have both positive and negative values. This indicates that the model can account for the backscatter of the turbulent energy, i.e. the energy is transferred from the small eddies to the large eddies. This happens in real flows locally at some instants of time although the long time-average energy transport is from the large eddies to the small eddies. The non-positive viscosity hence produced tends to cause a numerical instability or even a singularity. In a turbulent channel flow, it is a common procedure to average the denominator and the numerator in homogeneous directions [5, 8, 9]

$$C(y,t) = -\frac{\langle\mathscr{L}_{ij}M_{ij}\rangle_{xz}}{2\langle M_{ij}M_{ij}\rangle_{xz}} \tag{23}$$

3. NUMERICAL METHODS

3.1. The flow solver

The equations governing incompressible and isothermal Navier–Stokes flow are turned into a conservative form

$$\int_S \rho\mathbf{V}\cdot\mathbf{n}\,\mathrm{d}S = 0 \tag{24}$$

$$\frac{\partial}{\partial t}\int_V \rho u \,\mathrm{d}V + \int_S \left[\rho u \mathbf{V}\cdot\mathbf{n} + p n_x - \mu\left(n_x\frac{\partial u}{\partial x} + n_y\frac{\partial u}{\partial y} + n_z\frac{\partial u}{\partial z}\right)\right]\mathrm{d}S = 0$$

$$\frac{\partial}{\partial t}\int_V \rho v \,\mathrm{d}V + \int_S \left[\rho u \mathbf{V}\cdot\mathbf{n} + p n_y - \mu\left(n_x\frac{\partial v}{\partial x} + n_y\frac{\partial v}{\partial y} + n_z\frac{\partial v}{\partial z}\right)\right]\mathrm{d}S = 0$$

$$\frac{\partial}{\partial t}\int_V \rho w \,\mathrm{d}V + \int_S \left[\rho w \mathbf{V}\cdot\mathbf{n} + p n_z - \mu\left(n_x\frac{\partial w}{\partial x} + n_y\frac{\partial w}{\partial y} + n_z\frac{\partial w}{\partial z}\right)\right]\mathrm{d}S = 0$$

Above, $\mathbf{n} = n_x\mathbf{i} + n_y\mathbf{j} + n_z\mathbf{k}$ is a unit normal of the control volume face. The convection and diffusion terms are discretized with the second-order accurate Adams–Bashford scheme with respect to time, whereas the pressure is discretized with a first-order accurate Euler scheme:

$$\rho\mathbf{V}_{ijk}^{n+1} = \rho\mathbf{V}_{ijk}^{n} + \frac{\Delta t}{2V_{ijk}}(3\mathbf{R}_{ijk}^{n} - \mathbf{R}_{ijk}^{n-1}) - \frac{\Delta t}{V_{ijk}}\sum_{faces}(p\mathbf{S})^{n+1} \tag{25}$$

where $\mathbf{R}_{ijk}$ contains the convective and diffusive part. This method is the simplest multi-step method [12]. To compute Equation (25) a fractional-step approach is applied [13]. The computation is advanced in two parts:

$$\rho\mathbf{V}_{ijk}^{*} = \rho\mathbf{V}_{ijk}^{n} + \frac{\Delta t}{2V_{ijk}}(3\mathbf{R}_{ijk}^{n} - \mathbf{R}_{ijk}^{n-1}) \tag{26}$$

$$\rho\mathbf{V}_{ijk}^{n+1} = \rho\mathbf{V}_{ijk}^{*} - \frac{\Delta t}{V_{ijk}}\sum_{faces}(p\mathbf{S})^{n-1}. \tag{27}$$

For the latter equations, the mass balance is required for the control volume V_{ijk}. By performing the surface integral over the faces of the volume, a Poisson equation for the pressure is obtained.

$$A_{W,ijk}\,p_{i-1k} + A_{E,ijk}\,p_{i+1jk} + A_{S,ijk}\,p_{ij-1k} + A_{N,ijk}\,p_{ij+1k}$$
$$+A_{B,ijk}\,p_{ijk-1} + A_{T,ijk}\,p_{ijk+1} + A_{P,ijk}\,p_{ijk} = \sum_{faces}(\rho\mathbf{V}^{*}\cdot\mathbf{S})$$

$$\mathbf{A}\mathbf{p} = \mathbf{b} \tag{28}$$

where the coefficients in $\mathbf{A}$ are given by Majander [14]. The computation is started with an initial guess, which is used for both previous steps. Intermediate velocities $\mathbf{V}^{*}$ are computed and interpolated to the cell faces to calculate the mass balance.

The Poisson equation (28) is iterated for the pressures with an algebraic multigrid solver until the residual

$$L^2(p) = \frac{\sqrt{(\mathbf{A}\mathbf{p} - \mathbf{b})^2}}{\sqrt{\mathbf{b}^2}} \tag{29}$$

is reduced below 10^{-3}. This limit was found stringent enough to produce accurate results [14]. Finally, the new velocities can be corrected from Equation (27) to obtain the result at the new time step. Notice that no dissipation in the mass balance computation is used.

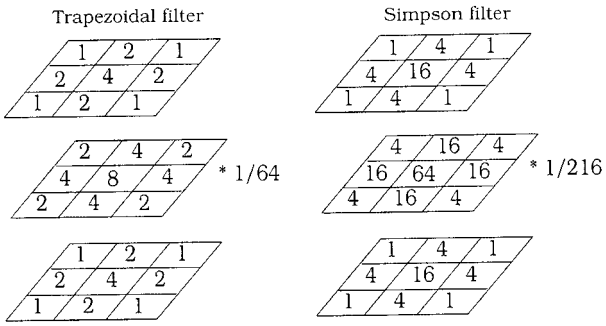

Figure 1. Trapezoidal and Simpson filters in three dimensions.

3.2. *Numerical test filters*

The filtering operation in one dimension over equidistant points a, b and c is defined as an integral

$$\overline{f(b)} = \int_a^c G(b-x')f(x')\,\mathrm{d}x' \tag{30}$$

The top-hat filter is then

$$\begin{aligned} G(b-x) &= \frac{1}{c-a} \quad \textit{if } |b-x| \leqslant \frac{c-a}{2} \\ G(b-x) &= 0 \qquad\quad \textit{if } |b-x| > \frac{c-a}{2} \end{aligned} \tag{31}$$

Let us consider a numerical integration using three points a, b and c. The trapezoidal rule leads to the following second-order accurate trapezoidal filter [12]

$$\overline{f(b)} = \tfrac{1}{4}\,[f(a) + 2f(b) + f(c)] \tag{32}$$

Application of the fifth-order accurate Simpson quadrature leads to the following fourth-order filter [12]

$$\overline{f(b)} = \tfrac{1}{6}\,[f(a) + 4f(b) + f(c)]. \tag{33}$$

In two and three dimensions, the filters can be applied in series in each dimension. The three-dimensional filters thus obtained are illustrated in Figure 1.

4. CHANNEL FLOW AT REYNOLDS NUMBER = 2800

The first test case is a fully developed turbulent flow in a channel with a bulk Reynolds number of 2800 defined as

$$Re_\mathrm{b} = \frac{U_\mathrm{b}\delta}{\nu} = 2800 \tag{34}$$

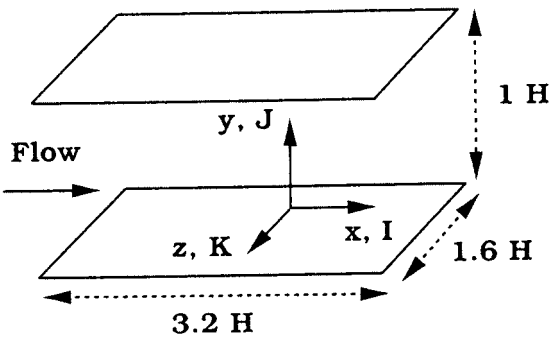

Figure 2. The computational domain in the channel flow. Periodic boundary conditions are applied in the streamwise (x) and the spanwise directions (z). Solid walls restrict the inhomogeneous direction (y).

where U_b is the bulk velocity and δ is half of the channel height H. This approximately equals a wall shear velocity based Reynolds number

$$Re_\tau = \frac{u_\tau \delta}{v} = 180 \tag{35}$$

where $u_\tau = \sqrt{\tau_w/\rho}$ is the wall shear velocity and τ_w is the wall shear stress. In these simulations the parameters have the following values: $H = 1\,m$, $U_b = 1\,\mathrm{m/s}$ and $v = 1.786 \times 10^{-4}\,\mathrm{m^2/s}$. Figure 2 shows a schematic picture of the channel. Periodic boundary conditions are applied in the steamwise and in the spanwise directions, where the lengths of the domain are $3.2H$ and $1.6H$, respectively. These distances are actually half of those used by Kim *et al.*, in their direct numerical simulation [15]. They utilized a spectral method and $192 \times 129 \times 160$ grid points in the x-, y- and z-directions, respectively. In the wall-normal direction, 64 cells are used and the height of the two closest cells next to the walls is $y^+ = 1$ in dimensionless units. This height can be approximated from the logarithmic law

$$\frac{U_b}{u_\tau} = \frac{1}{\kappa} \ln\left(\frac{u_\tau \delta}{v}\right) + B - \frac{1}{\kappa}$$

$$= \frac{1}{\kappa} \ln\left(\frac{U_b \delta}{v} \frac{u_\tau}{U_b}\right) + B - \frac{1}{\kappa}$$

$$\left(\frac{2}{c_f}\right)^{1/2} = \frac{1}{\kappa} \ln\left[Re_b \left(\frac{c_f}{2}\right)^{1/2}\right] + B - \frac{1}{\kappa} \tag{36}$$

where the following relation has been used:

$$\frac{U_b}{u_\tau} = \left(\frac{2}{c_f}\right)^{1/2} \tag{37}$$

Table I. The parameters of the grids used.

Grid	N_x	N_y	N_z	Δx^+	$\Delta y^+_{\min}$	$\Delta y^+_{\max}$	Δz^+
Coarse	16	64	16	71	1.0	16.8	36
Medium	32	64	32	36	1.0	16.8	18
Fine	64	64	64	18	1.0	16.8	9

Here, c_f is the skin-friction coefficient, which can be solved from Equation (36) after introducing the values $\kappa = 0.41$ and $B = 5.0$. Hence, u_τ is solved from Equation (37) and the dimensional distance from the wall in terms of y^+ can be solved from

$$y_n = \frac{y^+ v}{u_\tau} \tag{38}$$

The stretching ratio of the cells is 1.10 in the wall direction. The cell height next to the centreline is $16.8\Delta y^+_{\min}$. Calculations are carried out with three different grids, whose streamwise and spanwise cell densities vary. The parameters are given in Table I. The streamwise length of the box in dimensionless units is approximately $1140\Delta x^+$. The periodic boundary condition is set for all the variables. The pressure field is divided into two fields. A periodic field is solved from the Poisson equation just as in the spanwise direction. The bulk velocity is kept constant with a PID controller by adjusting a time-dependent gradient field, which is added to the streamwise convective flux in Equation (26). The controller is defined as

$$\begin{aligned} e &= (\dot{m}_{\text{set}} - \dot{m}_{\text{out}})/\dot{m}_{\text{set}} \\ \Delta p^{n+1} &= \Delta p^n + Kpe + K_I \int_{T^n - T_I}^{T^n} e \, \mathrm{d}t + K_D \frac{\mathrm{d}e}{\mathrm{d}t} \end{aligned} \tag{39}$$

where e is the relative mass flow error and Δp is the pressure difference driving the flow. $T_I = 10\Delta t$ is the integration time. After some experiments the coefficients were set as: $K_P = 100$, $K_I = 10/T_I = 1/\Delta t$, and $K_D = 20\Delta t$. The variation of the relative mass flow is of the order of 10^{-6} as the flow has developed.

4.1. Simulations with no Subgrid-Scale Model

The initial velocity profile for the simulation is

$$U_{ini} = U_{\text{b}}(1 - \cos(4\pi y/H)). \tag{40}$$

The flow seems to find a false steady solution, unless it is provoked with an initial condition that produces a lot of vorticity. This causes an earlier transition to turbulence and reduces the simulation time. The simulations with the coarse, medium and fine grids are called simulation 1, simulation 2 and simulation 3, respectively. The CFL numbers are 0.1, 0.1 and 0.2 in simulation 1, 2 and 3, respectively. The corresponding time-step sizes are then $0.008T$, $0.0048T$ and $0.0058T$, where $T = H/U_{\text{b}}$. In other words, the numbers of time steps for a bulk mass to pass the channel length are 400, 670 and 550, respectively. With simulation 1, the data

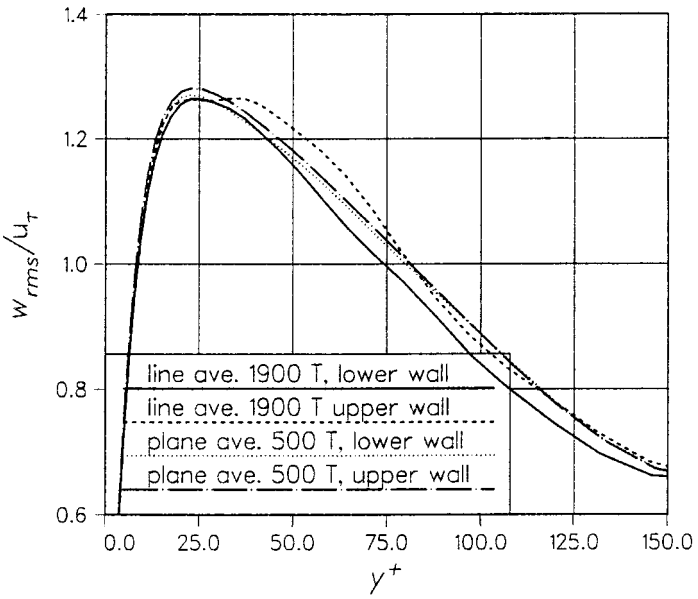

Figure 3. The dimensionless Reynolds stress w_{rms}/u_τ after averaging during $1900T$ along one line and $500T$ on the whole xz-plane.

acquisition is tested. The average of velocity u_i is collected continuously as

$$\bar{u}_{i,m} = [(m-1)\bar{u}_{i,m-1} + u_{i,m}]/m \tag{41}$$

where m is the number of the averaged instants. The averaged values of the Reynolds stresses are recorded in a similar manner:

$$\begin{aligned} u'_{i,m} &= u_{i,m} - \bar{u}_{i,m} \\ \overline{u'_i u'_{jm}} &= \left[(m-1)\overline{u'_i u'_{j_{m-1}}} + (u_{i,m} - \bar{u}_{i,m})(u_{j,m} - \bar{u}_{j,m})\right]/m \end{aligned} \tag{42}$$

where m is the number of the averaged instants. Since there are two homogeneous directions present, the data can be collected at each line normal to the walls and averaged at each time step. In more complex flows, this is hardly the case and the mean data has to be collected along one line. The upper and lower halves of the channel are collected separately in both cases. The single-line data collection was started at $t = 100T$ and it was continued until $t = 2000T$. As the averaging was done over the plane, it was stopped at $t = 600T$. As expected, with the latter method the Reynolds stresses converge faster, as seen in Figure 3. All the following computation utilized data collection over the whole xz-plane. The mean skin friction coefficient $c_f = 8.18 \times 10^{-3}$ is from the DNS conducted by Kim *et al.* [15], hereafter denoted by KMM. Simulation 1 underpredicts c_f by 18% giving $c_f = 6.70 \times 10^{-3}$ as an average. Simulation 2 underpredicts the mean $c_f = 7.86 \times 10^{-3}$ by 4%, while simulation 3 yields an accurate result, $c_f = 8.20 \times 10^{-3}$. The dimensionless velocity profiles are shown in Figure 4. Simulation 1

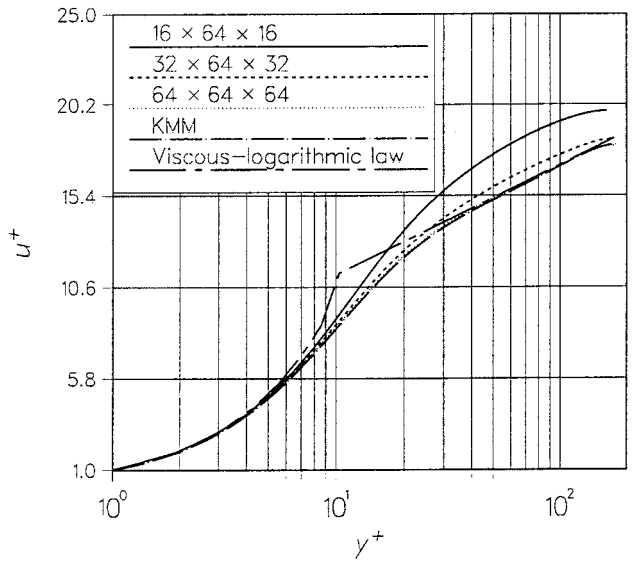

Figure 4. The dimensionless velocity profiles.

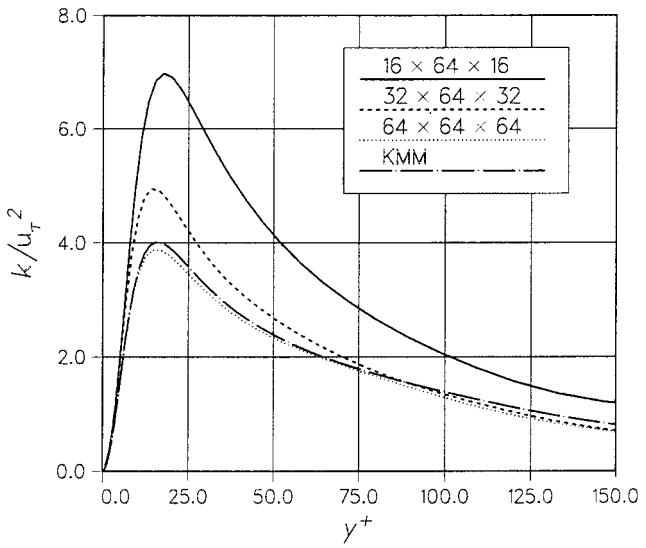

Figure 5. The kinetic energy normalized by the shear velocity k/u_τ^2.

does not predict as proper logarithmic region as simulation 2 does, although it does show some offset to the reference result. Simulation 3 coincides with the profile of KMM. Figures 5 and 6 present the Reynolds-averaged kinetic energy of turbulence normalized by the shear velocity; $k/u_\tau^2 = u_i' u_i'/2u_\tau^2$, and by the bulk velocity; $k/U_b^2 = u_i' u_i'/2U_b^2$, respectively. It can be

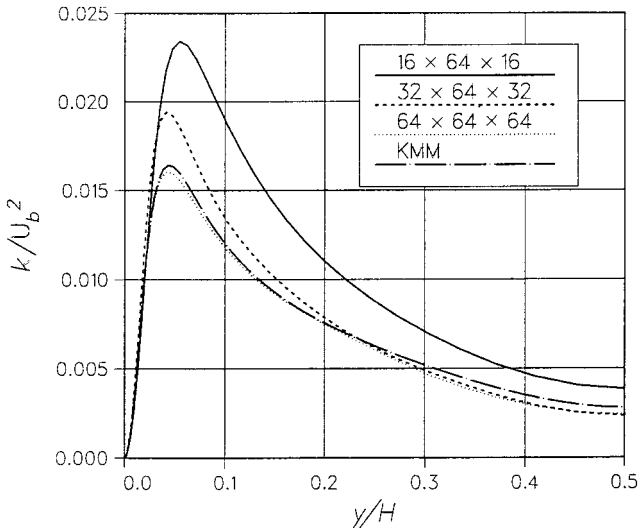

Figure 6. The kinetic energy normalized by the bulk velocity k/U_b^2.

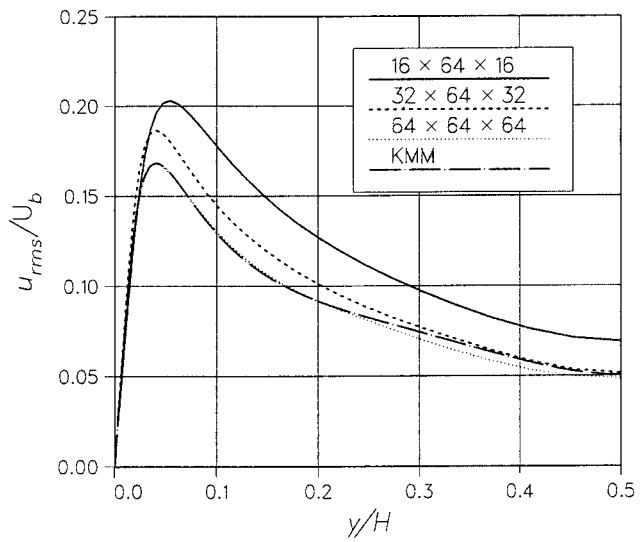

Figure 7. The rms fluctuations of u: $\sqrt{\overline{u'u'}}/U_b$.

observed that the normalization by the shear velocity somewhat exaggerates the differences between the results, since u_τ varies between the simulations. As the grid becomes finer, u_τ increases. Therefore, the rest of the results are mainly normalized by the bulk velocity.

Figures 7–10 show the resolved rms fluctuations; $\sqrt{\overline{u_i'u_{ij}'}}/U_b$, and the normalized Reynolds stress $\overline{u'v'}/U_b^2$.

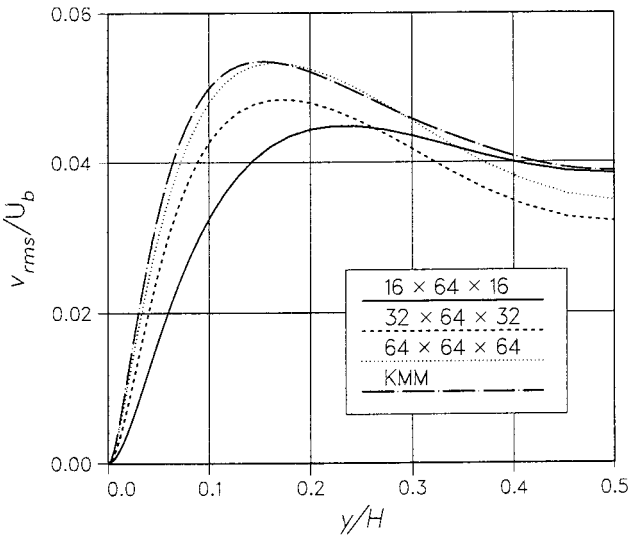

Figure 8. The rms fluctuations of v: $\sqrt{\overline{v'v'}}/U_b$.

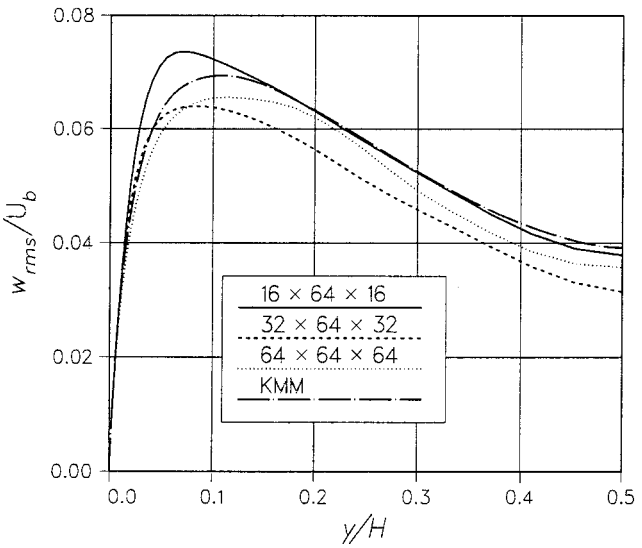

Figure 9. The rms fluctuations of w: $\sqrt{\overline{w'w'}}/U_b$.

The computations with the coarse and the medium grid overpredict the peak of the kinetic energy and underpredict the wall stress. The reason for this is likely an inadequate grid resolution. If the near-wall flow structures are not properly resolved, the effective shear stress on the wall is reduced. The fluctuations normal to the wall are underpredicted, which decreases the

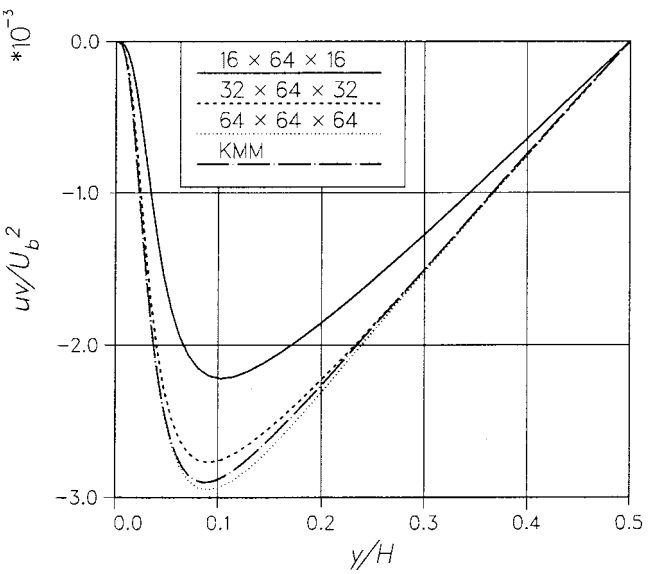

Figure 10. The dimensionless Reynolds stress $\overline{u'v'}/U_b^2$.

momentum transfer between the wall and the core flow. The dominant streamwise fluctuations grow and so does the resolved turbulent kinetic energy.

The fine-grid simulation predicts all the monitored quantities quite well, so it probably catches most of the eddies present in the flow. In this case, the largest deviations of the turbulent fluctuations are located in the core flow, when compared to the KMM results. The grid spacings are stretched geometrically in the wall-normal direction, which increases the cell sizes probably too much in the middle of the channel (Table I).

4.2. Simulations with subgrid-scale models

The channel flow computations are repeated with two different SGS models, a constant and a dynamic Smagorinsky model. The constant Smagorinsky model employs the van Driest damping function of Equation (11)

$$\nu_T = \left[C_s(1 - (e^{-y^+/25}))\Delta\right]^2 |\bar{S}|.$$

The value of C_s is 0.1 and the length-scale $\Delta = (\Delta x_1 \Delta x_2 \Delta x_3)^{1/3} = V^{1/3}$. The dynamic model computes the constant from Equation (22), after which it is averaged in the homogeneous x- and z-directions as in Equation (23):

$$C(y,t) = -\frac{\langle \mathscr{L}_{ij} M_{ij} \rangle_{xz}}{2\langle M_{ij} M_{ij} \rangle_{xz}}$$

As discussed in Section 2, the dynamic model needs the velocity field and the related quantities at two resolution levels. Two different filtering formulas are used, trapezoidal and Simpson

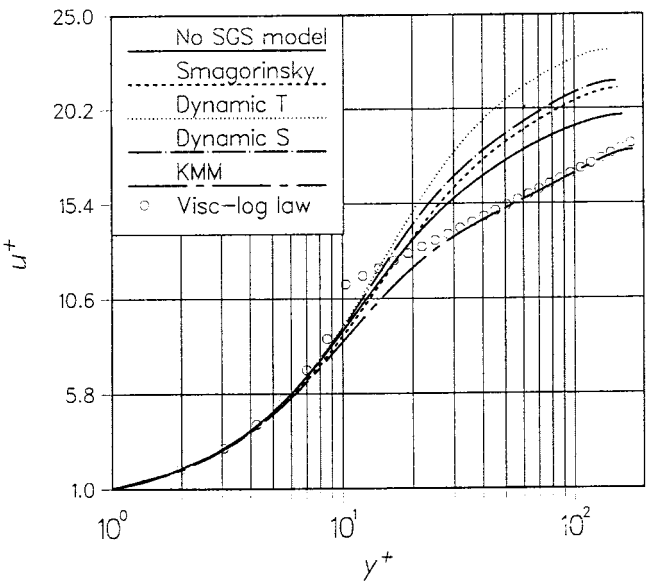

Figure 11. The dimensionless velocity profiles from the coarse-grid simulations.

filters, which are presented in Figure 1. In the following, the trapezoidal and Simpson implementations of the dynamic models are denoted as 'T' and 'S'. The filtering operation is done in all the three dimensions and no special treatment is used in the cell next to the solid surface. The total viscocity is restricted from being negative:

$$\nu_{\text{tot}} = \max(\nu + \nu_T, 0) = \max(\nu + C(y,t)\Delta^2|\bar{S}|, 0) \tag{43}$$

This limitation allows a backscattering effect whose magnitude is that of a molecular viscosity. The eddy viscocity is calculated after the pressure and the velocities have been solved at each time step.

The computations are initialized by the previous solutions with no SGS model. The time of the modelled coarse grid computations in $400T$. In Figures 11 and 12, the velocity profiles and the resolved kinetic energy from the simulations with the coarse grid are shown, respectively. In Figure 13 the resolved kinetic energy has been normalized by the shear velocity, which notably emphasizes the differences between the simulations. Also, the peak of the kinetic energy seems to have grown with the SGS models, whereas Figure 12 shows the opposite.

The corresponding normalized Reynolds stresses are shown in Figures 14–17. The additional turbulent viscosity laminarizes the flow even further and the velocity of the core is increased. The Smagorinsky model affects all the monitored quantities least and the dynamic model with the trapezoidal filtering most.

In Figure 18, the averaged eddy viscosity produced by the SGS models is shown. It is seen that the dynamic models predict greater eddy viscosity in the core of the flow than the Smagorinsky model. On the other hand, the viscosity from the dynamic model decreases faster

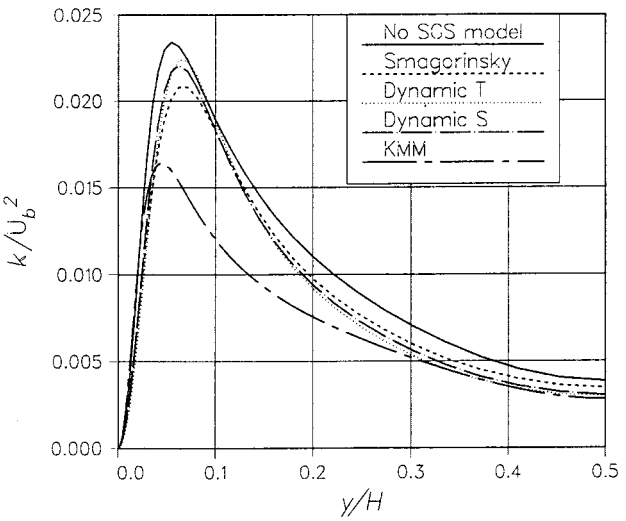

Figure 12. The kinetic energy normalized by the bulk velocity k/U_b^2. The results are from the coarse-grid simulations.

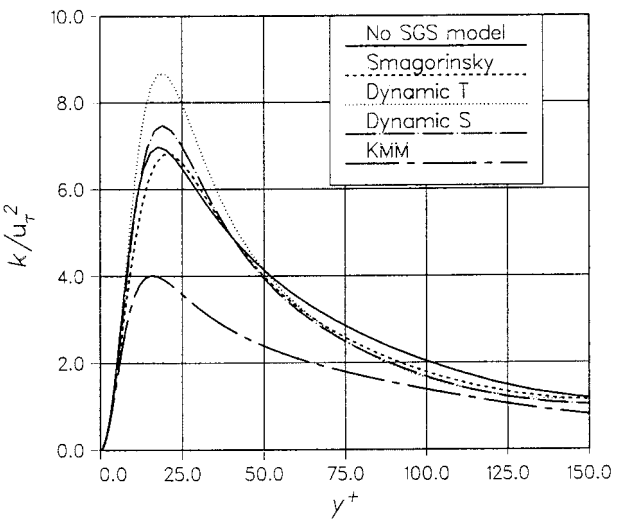

Figure 13. The kinetic energy normalized by the shear velocity k/U_τ^2. The results are from the coarse-grid simulations.

as the position moves towards the wall. A reference result is taken from the computations of Najjar and Tafti [9]. The reference solution has been obtained with the grid size $\Delta x^+ = 35.3$ and $\Delta z^+ = 8.8$. In the wall direction the grid size is stretched from $\Delta y^+_{\min} = 1.4$ to $\Delta y^+_{\max} = 14.1$.

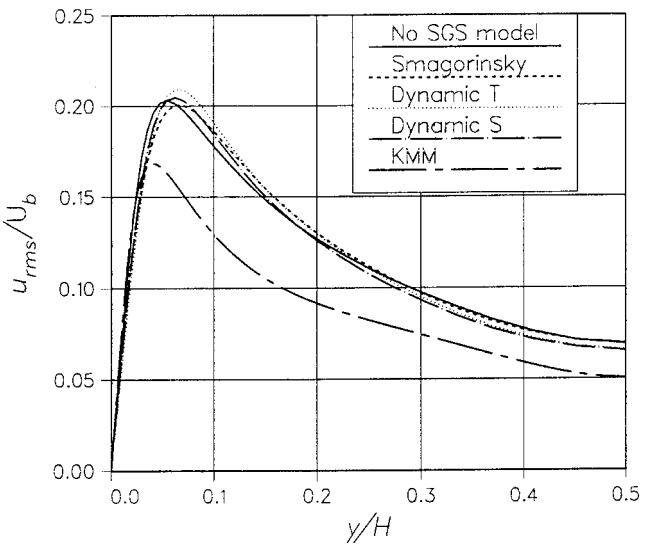

Figure 14. The rms fluctuations of u: $\sqrt{\overline{u'u'}}/U_b$. The results are from the coarse-grid simulations.

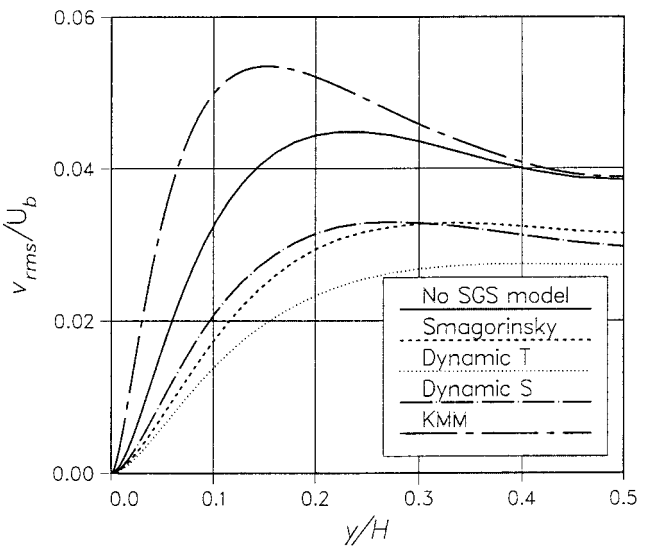

Figure 15. The rms fluctuations of v: $\sqrt{\overline{v'v'}}/U_b$. The results are from the coarse-grid simulations.

For the results shown here, Najjar and Tafti, hereafter denoted by NT, used a staggered non-dissipative Harlow–Welch scheme with several filtering formulas. In the figures, Cases 2 and 3 correspond to a trapezoidal filter with the length-scales $\hat{\Delta} = 2\Delta$ and $\hat{\Delta} = \sqrt{6}\Delta$, respectively. A high-order accurate seven-point filter is employed in Case 4 and the length-scale

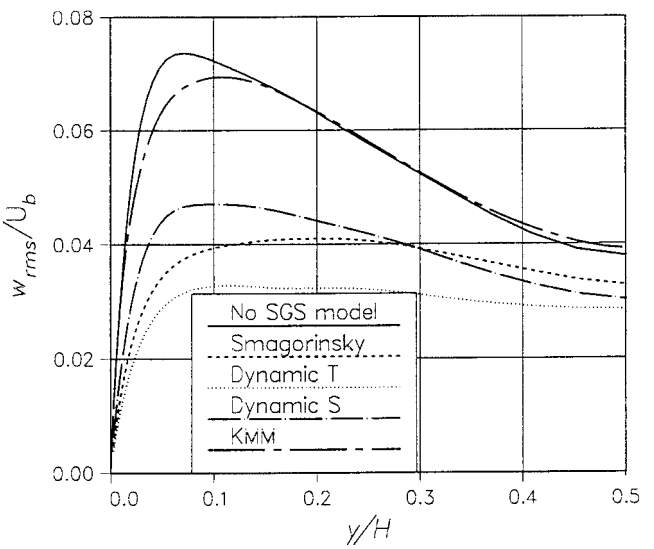

Figure 16. The rms fluctuations of w: $\sqrt{\overline{w'w'}}/U_b$. The results are from the coarse-grid simulations.

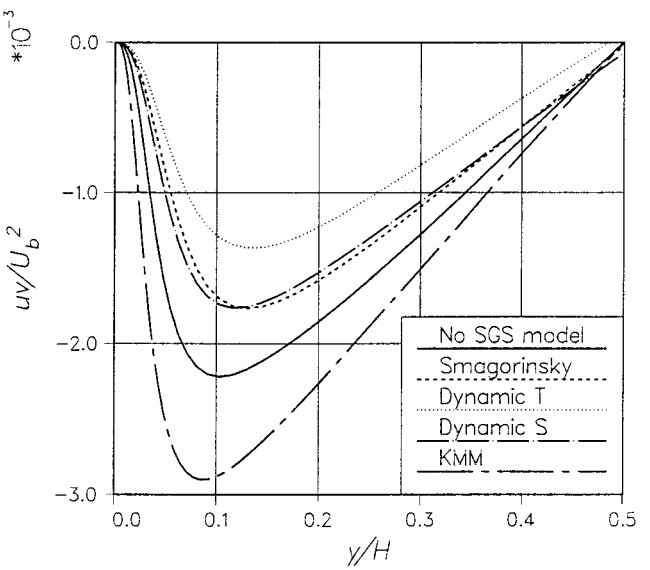

Figure 17. The dimensionless Reynolds stress $\overline{u'v'}/U_b^2$. The results are from the coarse-grid simulations.

$\hat{\Delta} = 2\Delta$. NT did not apply a filtering operation in the wall-normal direction. Figure 19 shows the dynamic coefficient C and the van Driest damping on the Smagorinsky coefficient. The Simpson filtering yields lower values than the trapezoidal one in the present computations. The longer length-scale applied by NT results in lower viscosity and the seven-point filtering

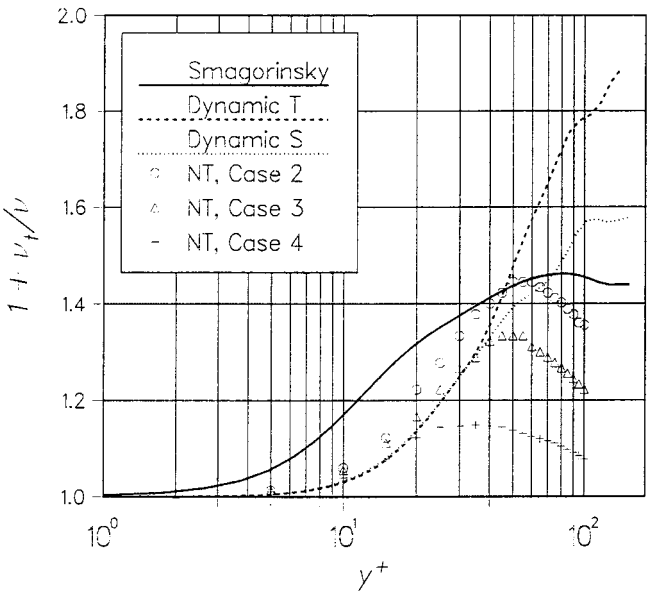

Figure 18. The eddy viscosity produced by the subgrid-scale models with the coarse-grid. The reference solution is from Najjar and Tafti [9].

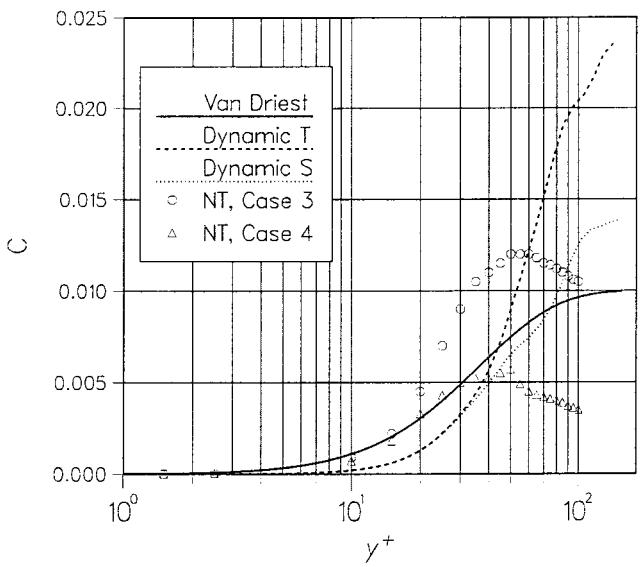

Figure 19. The subgrid-scale model coefficients with the coarse grid. The reference solution is from Najjar and Tafti [9].

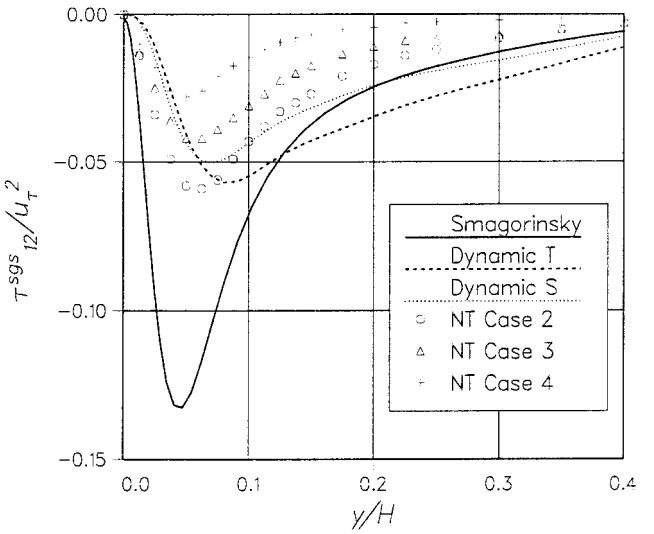

Figure 20. Distribution of the subgrid-scale Reynolds shear stress with the coarse grid. The reference solution is from Najjar and Tafti [9].

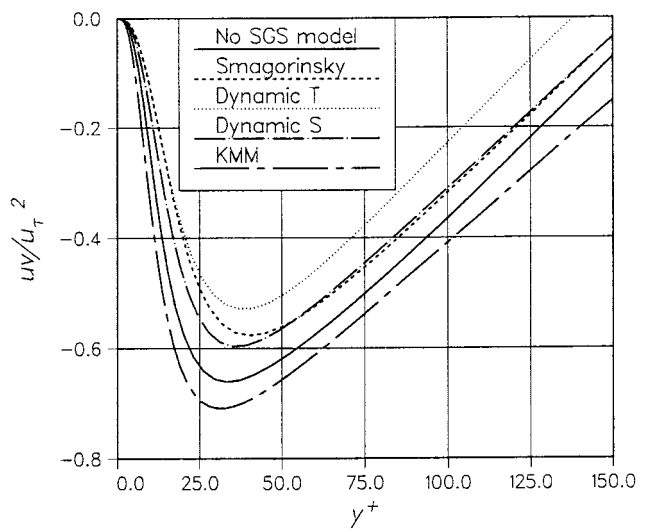

Figure 21. The dimensionless Reynolds stress $\overline{u'v'}/u_\tau^2$. The results are from the coarse-grid simulations.

reduces the value further. The distribution of the SGS Reynolds shear stress is shown in Figure 20. The peak value of the SGS stress is quite high with the Smagorinsky model, about 23% of the peak value of the resolved turbulent stress in Figure 21. For the dynamic models, the corresponding contribution is smaller, ca. 8% (S) and 11% (T).

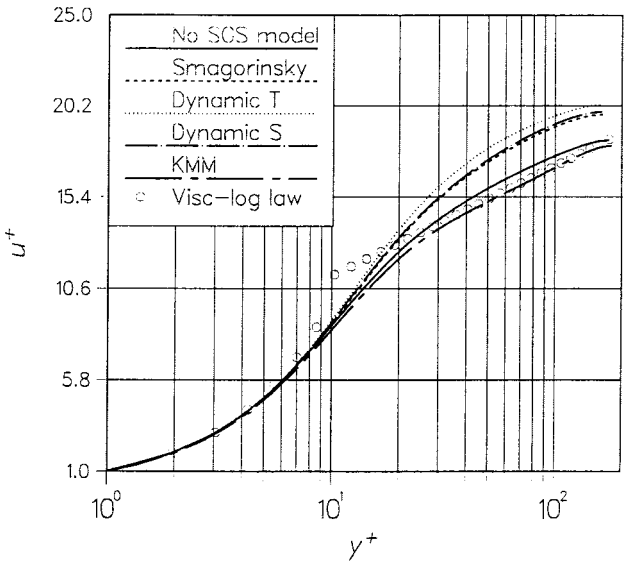

Figure 22. The dimensionless velocity profiles from the medium-grid simulations.

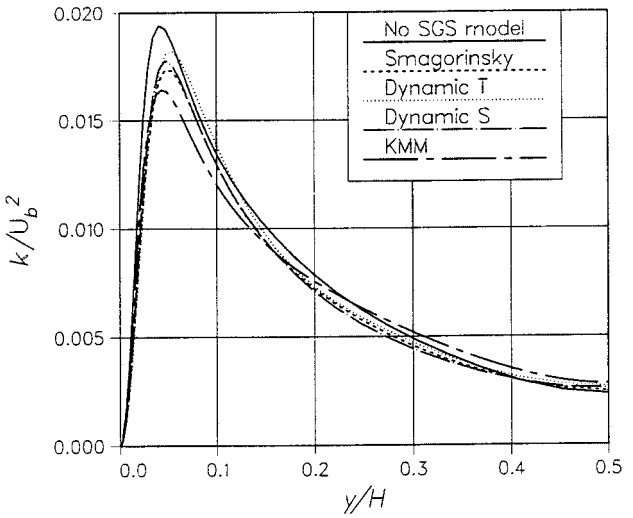

Figure 23. The kinetic energy normalized by the bulk velocity k/U_b^2. The results are from the medium-grid simulations.

The computing time for the modelled cases is $200\,T$ with the medium grid and $150\,T$ with the fine gird. Figures 22–31 show the results from the simulations with the medium grid and Figures 32–41 from the simulations with the fine grid. As a general observation, it can be stated that the skin friction is reduced by the SGS models, as seen in Table II. The reason for

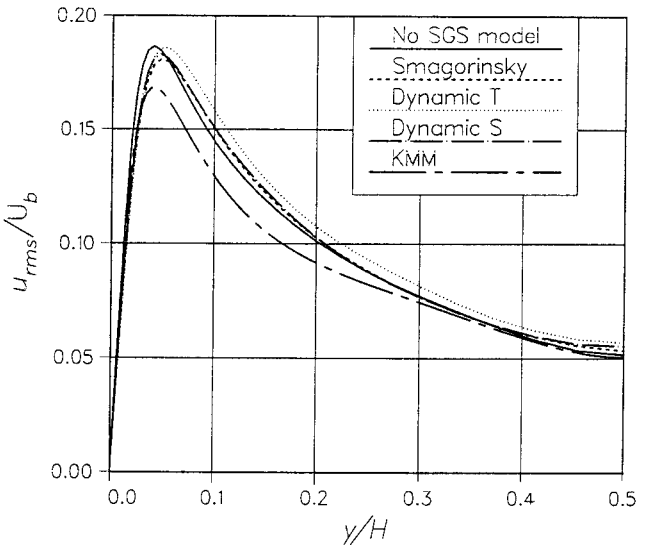

Figure 24. The rms fluctuations of u; $\sqrt{\overline{u'u'}}/U_b$. The results are from the medium-grid simulations.

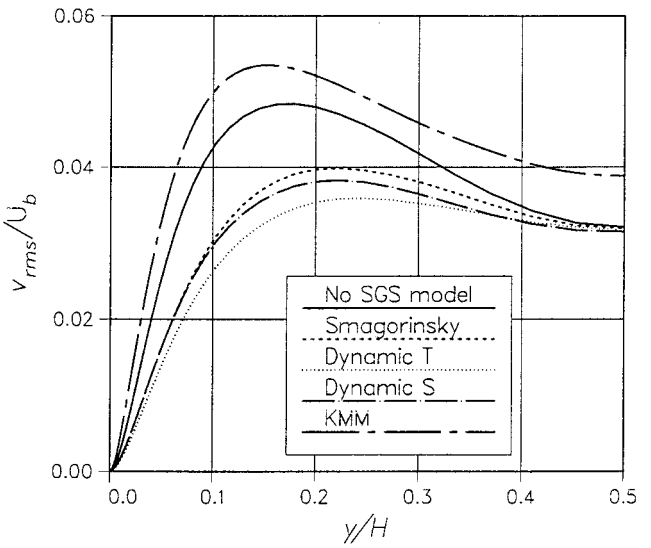

Figure 25. The rms fluctuations of v; $\sqrt{\overline{v'v'}}/U_b$. The results are from the medium-grid simulations.

this is that the stresses normal to the streamwise direction are damped, whereas the stresses in the streamwise direction remain almost unaffected in size. In order to improve the simulation the model should do the opposite. Furthermore, the 'correct' fine grid result is also altered. It appears that the model laminarizes the flow via eddy viscosity. The centre-line velocity

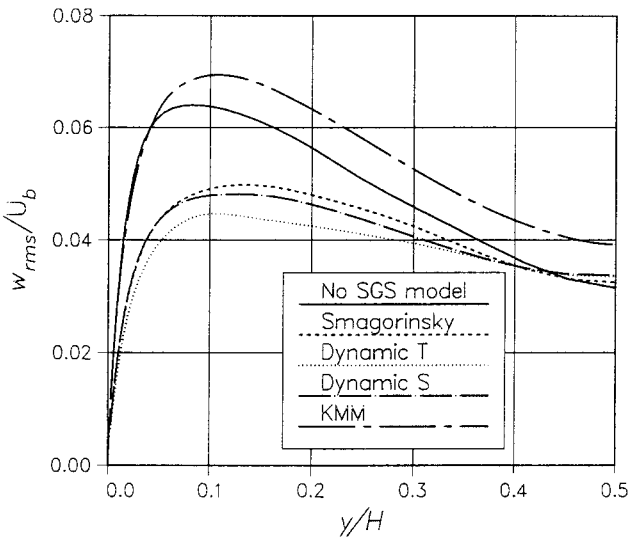

Figure 26. The rms fluctuations of w; $\sqrt{\overline{w'w'}}/U_b$. The results are from the medium-grid simulations.

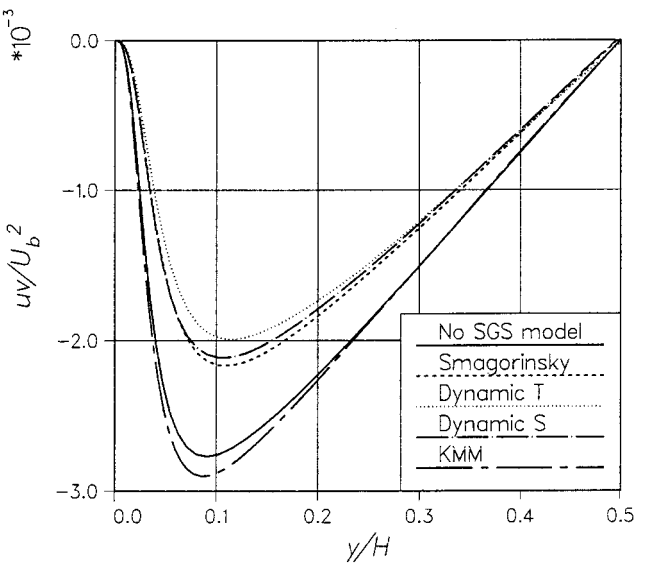

Figure 27. The dimensionless Reynolds stress $\overline{u'v'}/U_b^2$. The results are from the medium-grid simulations.

is increased in the modelled coarse-grid calculations. In other simulations the models did not significantly alter the averaged velocity profiles; the differences seen in the dimensionless velocity profiles are mainly due to the differences in the skin friction.

NT computed with two different grid sizes, which lie between the three grid sizes used in this study. With both grid sizes the resolved turbulent energy peak increased, as they turned

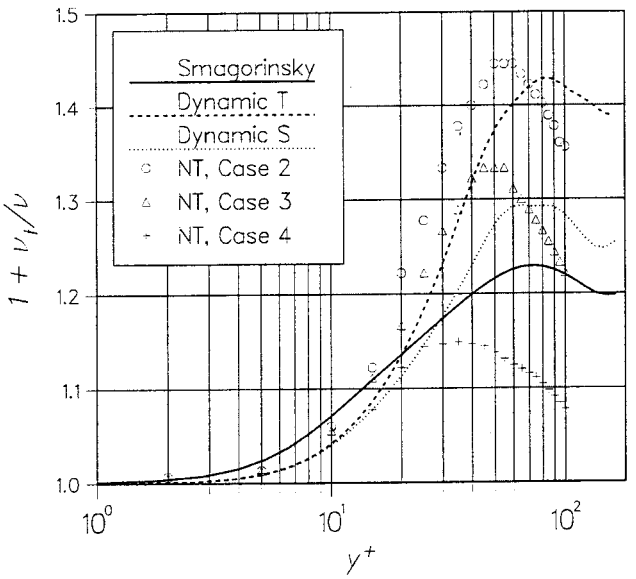

Figure 28. The eddy viscosity produced by the subgrid-scale models with the medium grid. The reference solution is from Najjar and Tafti [9].

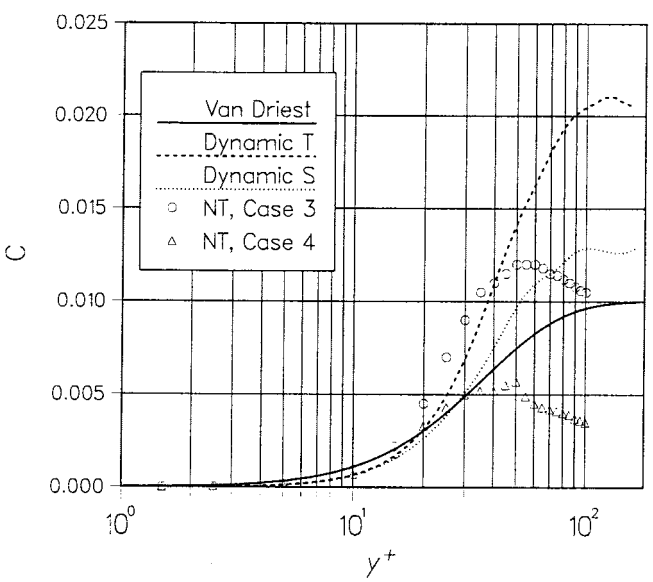

Figure 29. The subgrid-scale model coefficients with the medium grid. The reference solution is from Najjar and Tafti [9].

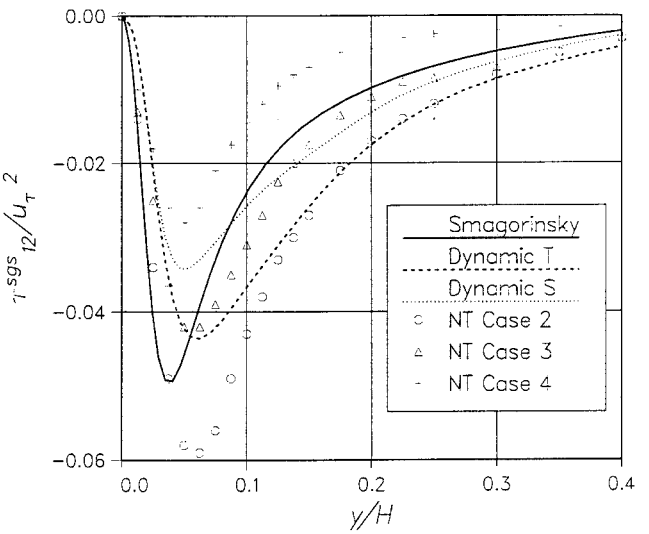

Figure 30. Distribution of the subgrid-scale Reynolds shear stress with the medium grid. The reference solution is from Najjar and Tafti [9].

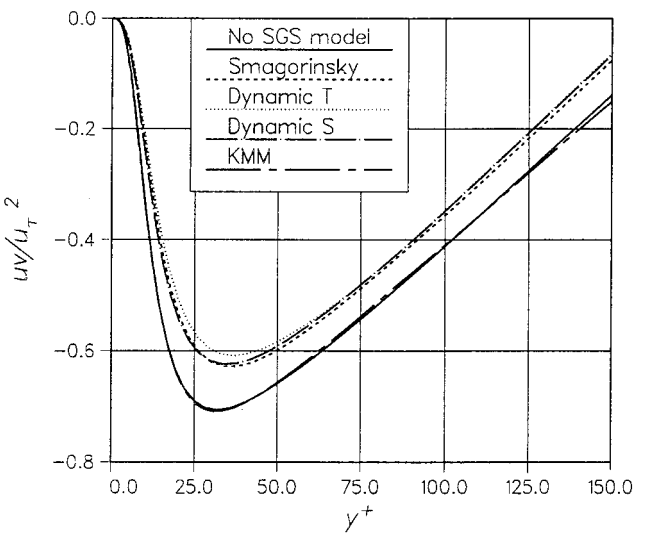

Figure 31. The dimensionless Reynolds stress $\overline{u'v'}/u_\tau^2$. The results are from the medium-grid simulations.

on the SGS model [9]. Their staggered code may be somewhat more accurate than our code using a co-located scheme. This could partly explain the fact that the resolved peak energy in their fine grid simulations is lower than that of the DNS result, whereas the peak value in

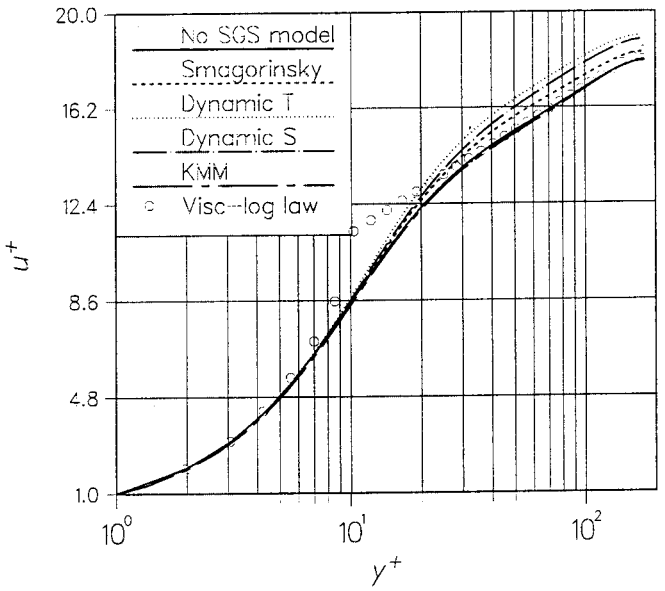

Figure 32. The dimensionless velocity profiles from the fine-grid simulations.

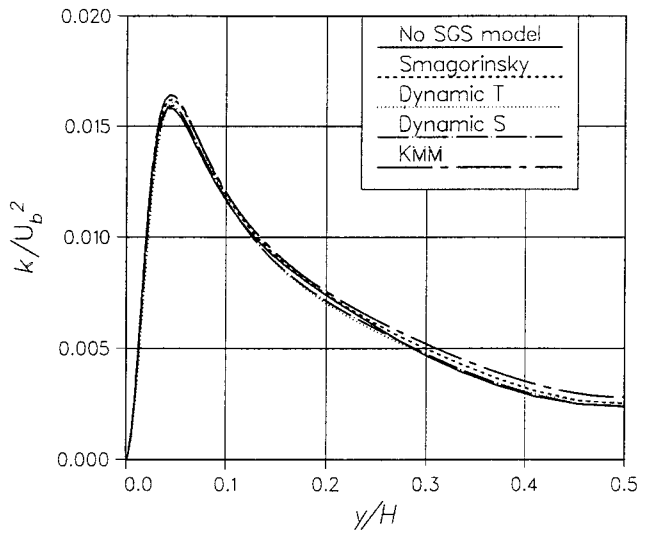

Figure 33. The kinetic energy normalized by the bulk velocity k/U_b^2.

their coarse grid simulation is comparable to that we obtained with our medium grid. Another reason that might enhance the effect is, that NT have normalized their results with the friction velocity, which varies slightly between their simulations.

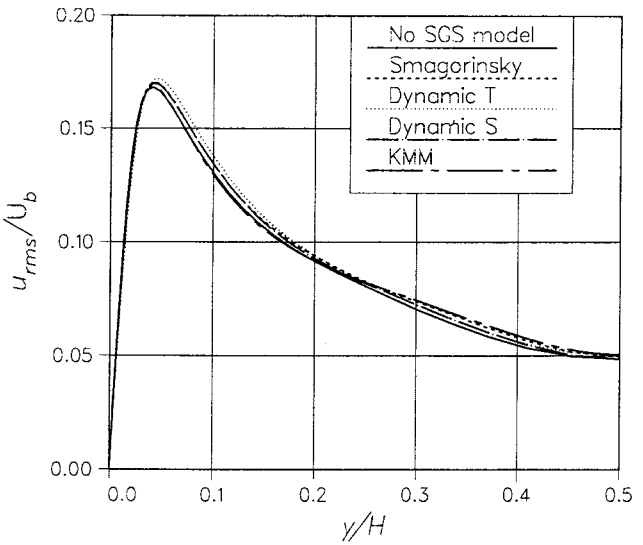

Figure 34. The rms fluctuations of u; $\sqrt{\overline{u'u'}}/U_b$. The results are from the fine-grid simulations.

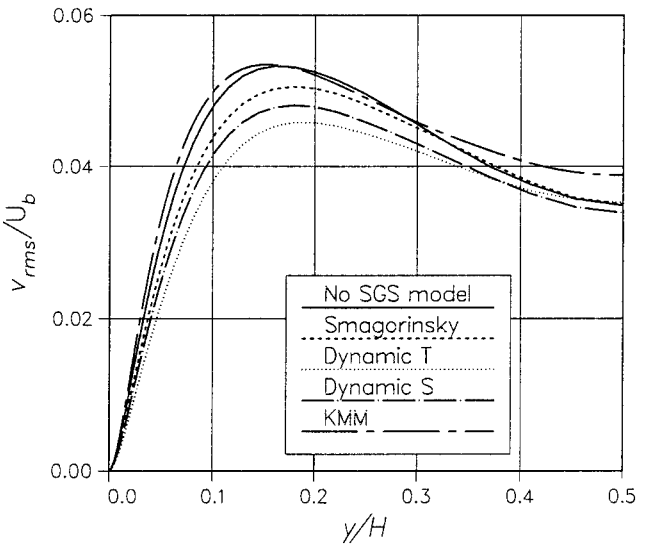

Figure 35. The rms fluctuations of v; $\sqrt{\overline{v'v'}}/U_b$. The results are from the fine-grid simulations.

The trapezoidal filtering operation procures larger values for the dynamic coefficient and the eddy viscosity than the Simpson filtering. The influence of the SGS model is reduced, however, as the mesh becomes finer. With the fine grid, the peak SGS shear stress is now

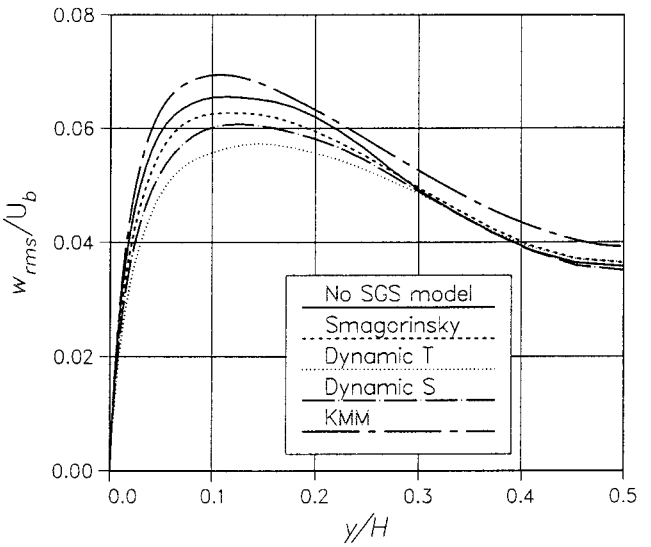

Figure 36. The rms fluctuations of w; $\sqrt{\overline{w'w'}}/U_b$. The results are from the fine-grid simulations.

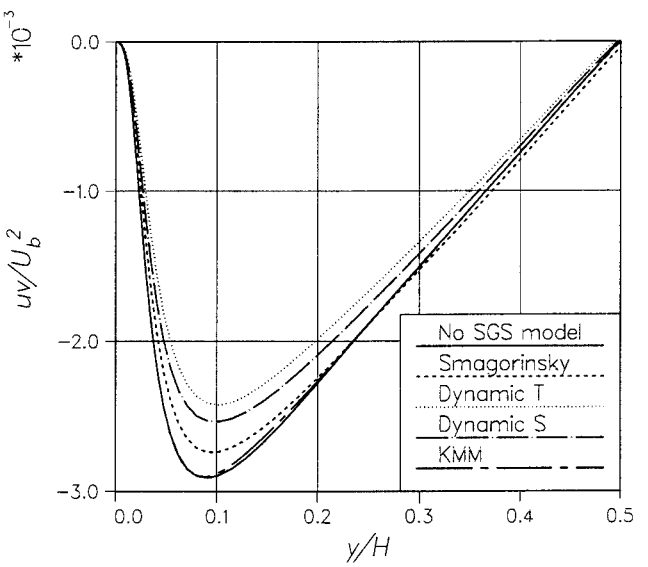

Figure 37. The dimensionless Reynolds stress $\overline{u'v'}/U_b^2$. The results are from the fine-grid simulations.

3–4% of the resolved stress peak shown in Figures 40 and 41, respectively. The magnitudes of the eddy viscosities in the present medium-grid simulations are quite similar to the NT results, shown in Figure 28.

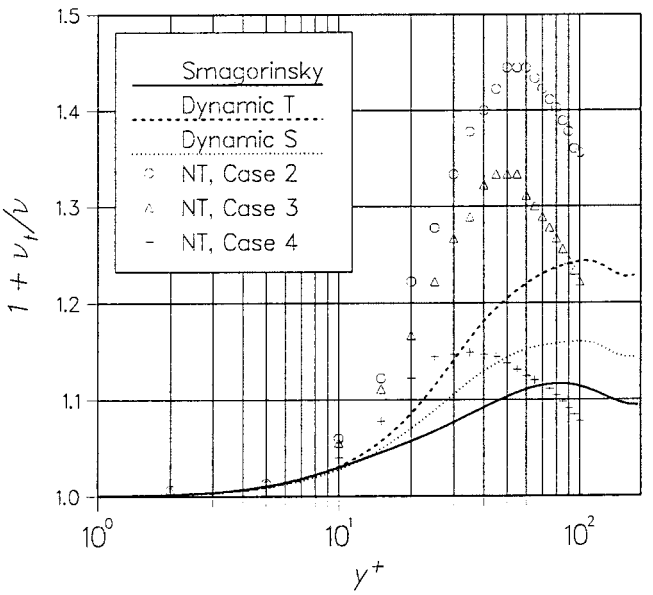

Figure 38. The eddy viscosity produced by the subgrid-scale models with the fine grid. The reference solution is from Najjar and Tafti [9].

5. CHANNEL FLOW AT REYNOLDS NUMBER 12 500

The second test case is a fully developed turbulent flow in a channel with a bulk Reynolds number of 12 500 defined as

$$Re_b = \frac{U_b \delta}{\nu} = 12\,500 \tag{44}$$

where U_b is the bulk velocity and δ is half of the channel height H. In these simulations the parameters have the following values: $H = 1\,\mathrm{m}$ $U_b = 1\,\mathrm{m/s}$ and $\nu = 4 \times 10^{-5}\,\mathrm{m^2/s}$. As in the previous case, periodic boundary conditions are applied in the streamwise and in the spanwise directions, where the lengths of the domain are $2.0H$ and $1.0H$, respectively. In the wall-normal direction, 64 cells are used and the height of the two closest cells next to the walls is approximated to be around $y^+ = 2$ from the logarithmic law (36). The stretching ratio of the cells is ca. 1.129 in the wall direction. The cell height next to the centre-line becomes then 76 in wall units. The streamwise length and the spanwise width of the box in dimensionless units are 2602 and 1301 in wall units, respectively. Both directions are divided into 32 cells so that the cell area normal to the wall is 80×40 in wall units.

5.1. Results

Simulations are conducted with no SGS model, with the constant and the dynamic Smagorinsky models, as before. All the simulations are run during the time of $250\,T$ where $T = H/U_b$. With the initial profile (40) the transition occurs at the time interval $15\,T$–$25\,T$. The statistics

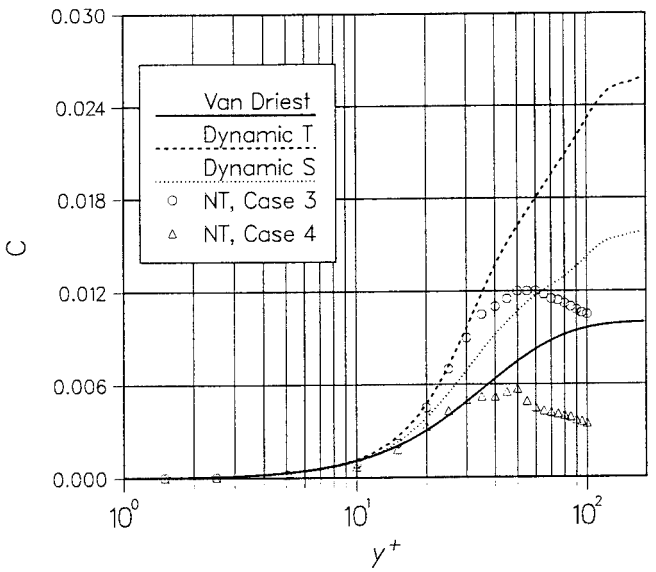

Figure 39. The subgrid-scale model coefficients with the fine grid. The reference solution is from Najjar and Tafti [9].

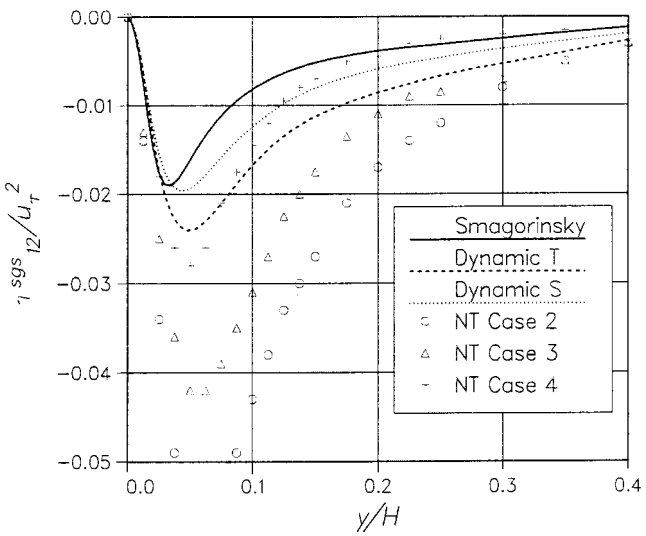

Figure 40. Distribution of the subgrid-scale Reynolds shear stress with the fine grid. The reference solution is from Najjar and Tafti [9].

are gathered during the last 200 T. The CFL number is 0.15 in every simulation. The time-step sizes become then 0.00478 T, 0.00607 T, 0.00579 T and 0.00583 T in the computations with no model, the constant Smagorinsky model, the trapezoidally and Simpson filtered dynamic

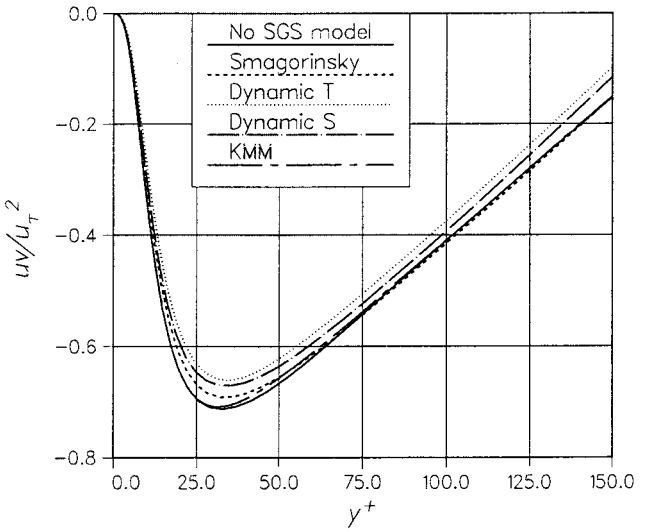

Figure 41. The dimensionless Reynolds stress $\overline{u'v'}/u_\tau^2$. The results are from the fine-grid simulations.

Table II. The mean skin-friction coefficient c_f and the normalized centre-line velocity U_c/U_b. Channel flow with $Re_b = 2800$.

Case	No SGS model		Smagorinsky		Dynamic T		Dynamic S	
	c_f	U_c/U_b	c_f	U_c/U_b	c_f	U_c/U_b	c_f	U_c/U_b
KMM [15]	8.18×10^{-3}	1.16						
Coarse	6.70×10^{-3}	1.151	6.05×10^{-3}	1.175	5.28×10^{-3}	1.177	5.76×10^{-3}	1.173
Medium	7.86×10^{-3}	1.156	6.93×10^{-3}	1.159	6.46×10^{-3}	1.158	6.79×10^{-3}	1.157
Fine	8.20×10^{-3}	1.160	7.85×10^{-3}	1.157	7.37×10^{-3}	1.154	7.54×10^{-3}	1.162

Table III. The mean skin-friction coefficient c_f and the normalized centre-line velocity U_c/U_b. Channel flow with $Re_b = 12\,500$.

Case	$Re_c = 13800$[16]	No SGS model	Smagorinsky	Dynamic T	Dynamic S
c_f	5.55×10^{-3}	4.59×10^{-3}	4.52×10^{-3}	3.91×10^{-3}	4.11×10^{-3}
U_c/U_b	1.135	1.106	1.111	1.097	1.105

Smagorinsky models, respectively. It is shown in Figure 42 that the simulations predict flatter profile than the measured profile by Hussain and Reynolds at $Re_c = 13800$ [16]. Here Re_c refers to the Reynolds number that is based on the centre-line velocity. The friction coefficients are 17–30% lower than the measured value as seen in Table III. The dimensionless profiles in Figure 43 show a logarithmic region and the offset is due to underpredicted friction. The resolved Reynolds stresses are presented in Figures 44–46. The reference results are measured by Wei and Willmarth at $Re_c = 14\ 914$ [17]. The results from the non-modelled computation deviate from the other results, especially in the core flow, and did not converge

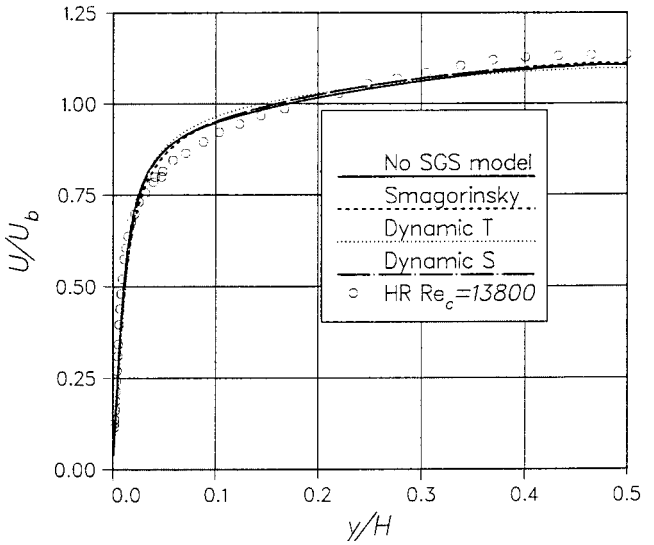

Figure 42. The velocity profiles from the channel flow at Reynolds number 12 500. The reference measurements by Hussain and Reynolds [16].

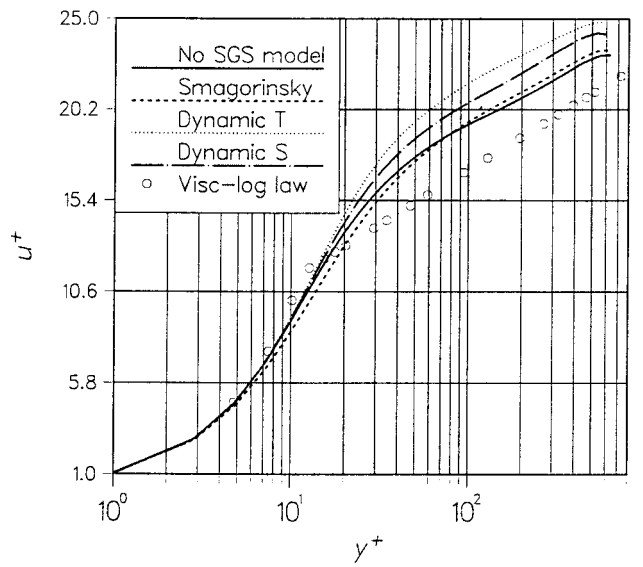

Figure 43. The dimensionless velocity profiles from the channel flow at Reynolds number 12 500.

properly. The inspection of the instantaneous flow field reveals that the solution is oscillating non-physically. In the core, where the cells are large, the instability affects most severely. The constant Smagorinsky model predicts the resolved quantities slightly better than the dynamic models do. The streamwise fluctuations are overpredicted and the fluctuations normal

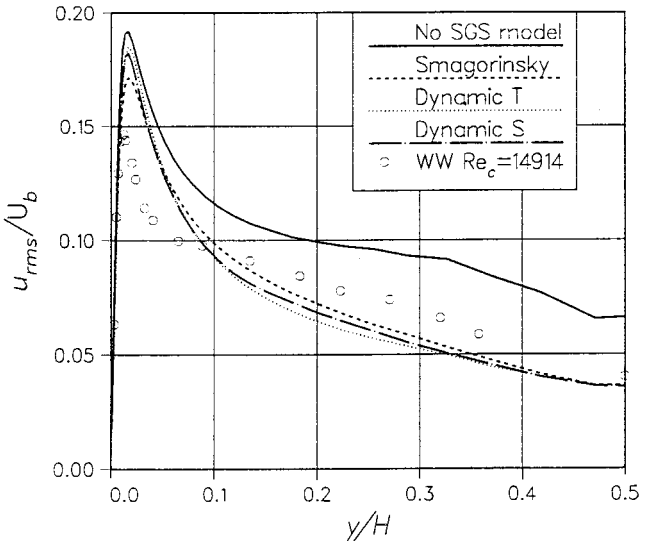

Figure 44. The rms fluctuations of u; $\sqrt{\overline{u'u'}}/U_b$ at $Re_b = 12\,500$. The reference measurements by Wei and Willmarth [17].

to the wall are underpredicted as in the case $Re_b = 2800$. The subgrid scale shear stresses τ_{12}^{sgs}/U_b^2 are plotted with the resolved turbulent shear stresses uv/U_b^2 in Figure 47. The constant Smagorinsky model computes a peak that is three times higher than the ones from the dynamic model. The ratios of the peaks of the SGS stresses to the peaks of the resolved turbulent stresses are close to those from the computations at $Re_b = 2800$ with the coarse grid. The peak is also localized closer to the wall ($\sim$ 15 in wall units) than those predicted by dynamic models ($\sim$ 30 in wall units). The eddy viscosity behaves as in the lower Reynolds number case. Smagorinsky model computes the lowest viscosity in the core flow, whereas the dynamic models predict lower eddy viscosity in the domain near the wall ($y^+ < 50$).

6. DISCRETIZATION ERRORS

The discretization errors may influence the result even more than the SGS model. Vreman *et al.* studied this by computing a DNS of a two-dimensional compressible mixing layer [18,19]. The flow field at one instant of time was filtered and the exact subgrid-scale stresses were compared to the discretization error obtained by estimating accurate derivatives to those of the coarse LES grid. They found that the discretization error with a second order scheme is larger than the SGS model output, if the filtering length is smaller than ca. 2 grid-spacing lengths.

Here we follow a similar procedure as Vreman *et al.* in order to compare the discretization error and the subgrid term. The case at $Re_b = 2800$ is computed with a dense grid size of $128 \times 64 \times 128$. The filtering operation to this field, which is assumed to an accurate DNS

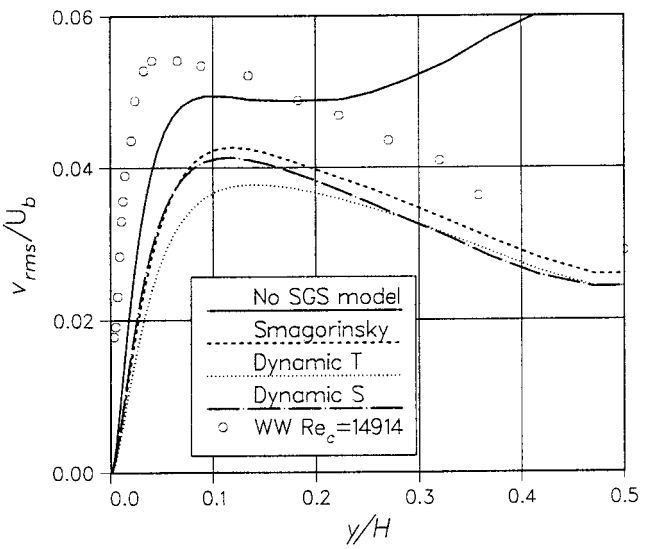

Figure 45. The rms fluctuations of v; $\sqrt{\overline{v'v'}}/U_b$ at $Re_b = 12\,500$. The reference measurements by Wei and Willmarth [17].

result, yields

$$\frac{\partial \overline{u_i u_j}}{\partial x_j} = \frac{\partial \bar{u}_i \bar{u}_j}{\partial x_j} + \frac{\partial \tau_{ij}}{\partial x_j} \tag{45}$$

where the SGS stesses are given by

$$\tau_{ij} = \overline{u_i u_j} - \bar{u}_i \bar{u}_j \tag{46}$$

The above derivatives are estimated with a fourth-order scheme in the homogeneous directions. In the wall normal directions then derivatives are estimated with a second-order scheme, which takes into account the grid stretching. In a coarse LES grid the discretization error is introduced also in the pressure term, whereas the diffusion term is ignored, since it is smaller by the magnitude of the Reynolds number. The relation of the discretized i-direction convective terms between two resolutions can be written as

$$\frac{\partial \bar{u}_i \bar{u}_j}{\partial x_j} + \frac{1}{\rho}\frac{\partial \bar{p}}{\partial x_i} = \frac{\delta \bar{u}_i \bar{u}_j}{\delta x_j} + \frac{1}{\rho}\frac{\delta \bar{p}}{\delta x_i} + \varphi_i, \tag{47}$$

where $\delta/\delta x_i$ denotes for the second-order finite volume operator used in the simulations and φ_i is the error between the fine and coarse level approximations.

An instantaneous flow field was filtered by a trapezoidal formula by using 6 and 10 cells in each homogeneous direction. The filters are then 5 and 9 grid-spacings wide, respectively. The filtered variables coincide at the wall-normal plane in the gird nodes of the dense drid, and at the cell center nodes of the $32 \times 64 \times 32$ grid. At the coarse mesh level the filters are 1.25 and 2.25 grid spacings wide, respectively. In the wall normal direction the variables are not filtered. The accurate subgrid-scale stresses can be defined from Equation (46). The

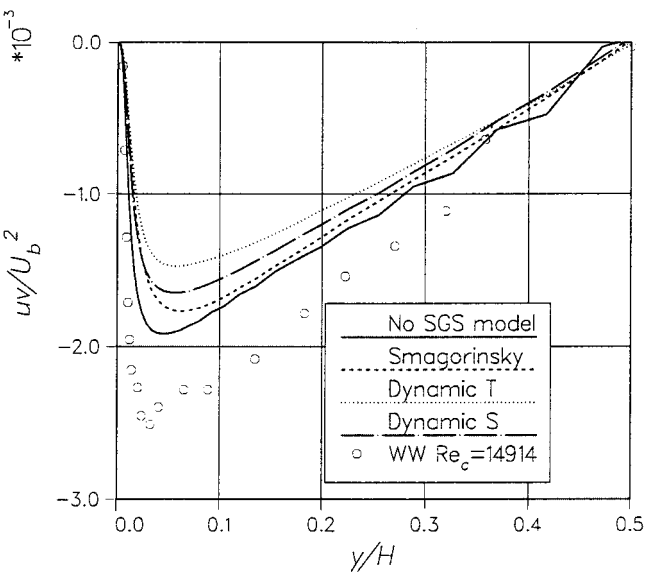

Figure 46. The resolved Reynolds stress $\overline{u'v'}/U_b^2$ at $Re_b = 12\,500$. The reference measurements by Wei and Willmarth [17].

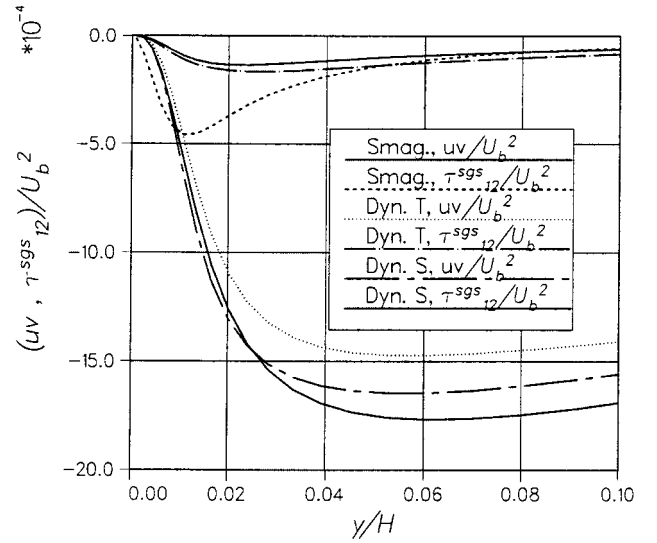

Figure 47. The subgrid scale stress τ_{12}^{sgs}/U_b^2 and resolved turbulent stress $\overline{u'v'}/U_b^2$ at $Re_b = 12\,500$.

discretization error φ_i can be estimated from Equation (47) in each co-ordinate direction. The L_2-norms of φ_i and $\partial\tau_{ij}/\partial x_j$ are presented in Figures 49–51. The quantities are computed over the xz-planes at one instant of solution.

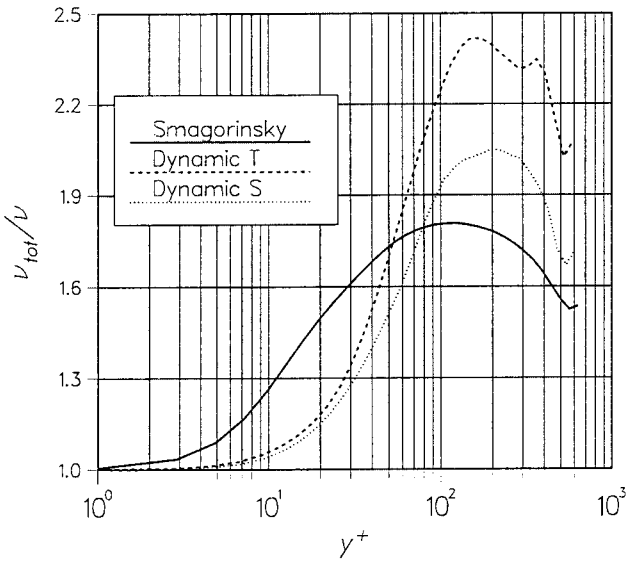

Figure 48. The scaled subgrid scale viscosity $(\nu + \nu_t)/\nu$ at $Re_b = 12\,500$.

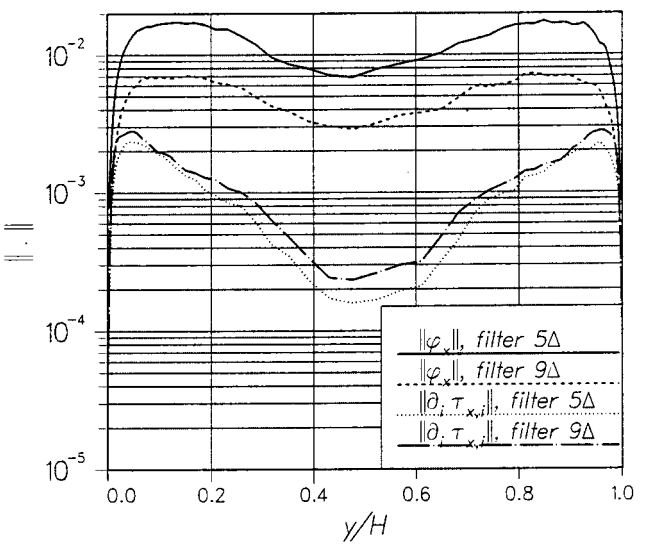

Figure 49. The L_2-norm of the estimated discretization error $\|\varphi_x\|$ and the subgrid term $\|\partial\tau_{x,x_i}/\partial x_i\|$ in the streamwise direction.

The discretization errors are larger than the subgrid term by a factor of 10. The longer filter increases the subgrid term, but the numerical error still dominates in most of the domain. Only in the vicinity of the wall the subgrid term becomes larger, especially in the wall normal

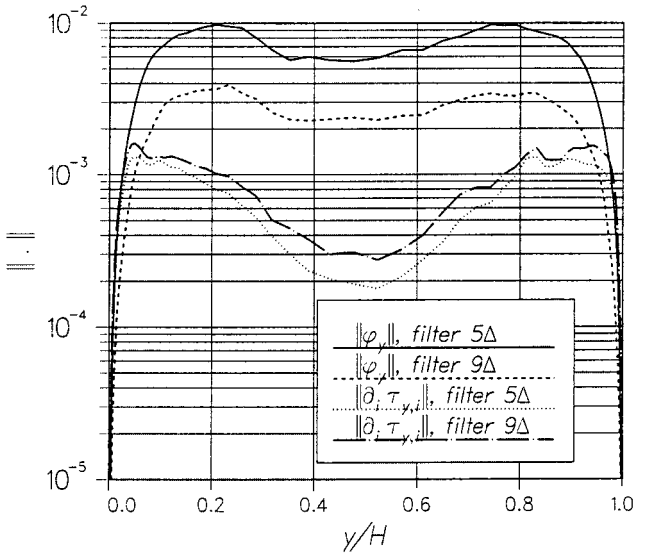

Figure 50. The L_2-norm of the estimated discretization error $\|\varphi_y\|$ and the subgrid term $\|\partial\tau_{y,x_i}/\partial x_i\|$ in the wall normal direction.

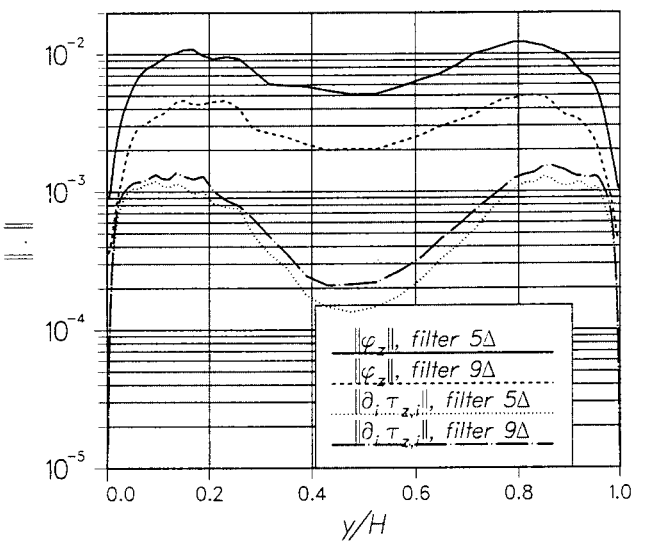

Figure 51. The L_2-norm of the estimated discretization error $\|\varphi_z\|$ and the subgrid term $\|\partial\tau_{z,x_i}/\partial x_i\|$ in the spanwise direction.

equation as seen in Figure 50. Vreman *et al.* found that in a two dimensional mixing layer the subgrid term is about 25% of the discretization error as the filter width is equal to the grid size. As the filter width is twice the grid size, the subgrid term is approximately equal

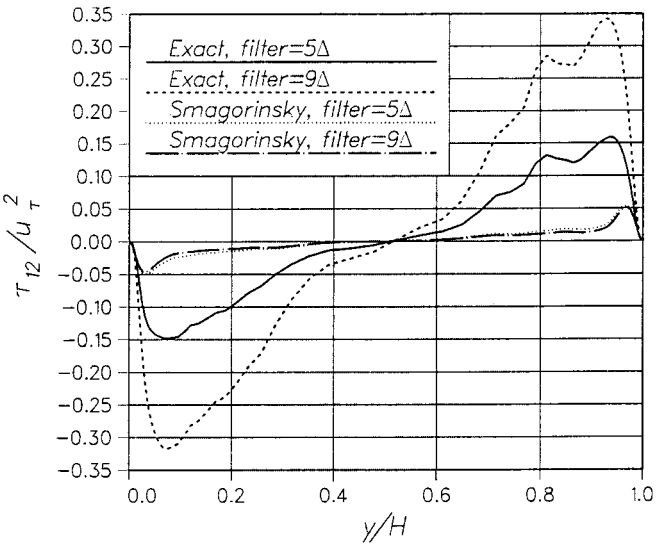

Figure 52. The subgrid shear stress τ_{12}/u_τ^2 calculated exactly and by the Smagorinsky model.

to the numerical error. The initial Reynolds number based on the vorticity thickness was 200 and the final Reynolds number was about 1000 in their calculation [18,19]. Even a perfect SGS model cannot produce an accurate solution in the presence of dominant numerical errors.

The shear stress components of Smagorinsky model were compared to the exact ones. The model output was computed at the fine grid level by using the filtered variables and the fourth-order accurate schemes in order to minimize the numerical errors. Figure 52 shows the exact and the modelled shear stress component τ_{12}/u_τ^2. It is seen that the exact stress component is considerably larger than the modelled one. The subgrid shear stress from the actual simulation with the medium grid show in Figure 30 is as large as the modelled subgrid shear stress computed here. By increasing the filter width, the exact stress is increased proportionally, whereas the modelled stress stays nearly constant. The correlation coefficient is around 0.4 between the exact and the modelled τ_{12}. The coefficient is normalized by the magnitudes of the stresses. For the other shear stresses there exists hardly any correlation. The low correlations between the exact and Smagorinsky stresses have previously been confirmed by Vreman *et al.* [19] in plane mixing layer flow and by Clark *et al.* [20] in homogeneous isotropic turbulence.

7. CONCLUSIONS

The channel flow at $Re_b = 2800$ was computed first with no subgrid-scale (SGS) model by employing three different mesh sizes. The coarse-grid calculations overpredicted the peak of the turbulent energy and underpredicted the wall stress. It is known from the experiments and the simulations, that in the spanwise direction there exist streaks of high and low speed fluid with a mean spacing of 100 wall units [15]. It is probable that the coarse gird, with a spanwise node spacing of 36 wall units, is unable to capture these near-wall eddies correctly. With the

fine grid, all the monitored quantities are quite close to those from the reference DNS. As the SGS models are turned on, the eddy viscosity damps the flow and the wall stresses decrease further. In addition, the result from the fine grid is altered correspondingly. The eddy viscosity from all the SGS models is decreased with the decreasing mesh spacing, but apparently this 'laminarization' process is inadequate for all the SGS models applied. Najjar and Tafti [9] used a staggered mesh with a second-order Harlow–Welch scheme and a fifth-order upwind biased scheme for the advection term in their study. They concluded that the dynamic model improved the prediction capability of their result, when used with the Harlow–Welch scheme and with a minimum resolution that would capture energy producing mechanisms. This study, performed with a co-located mesh and a second-order central discretization, indicated no improvements at any grid level tested.

It was observed that normalizing the results by the shear velocity is not proper, since it varies from one calculation to another. Ignoring this fact might lead to false conclusions, especially in assessing the influence of the SGS model on the resolved turbulent quantities.

The filtering operation affects the model output; in the current dynamic models the top-hat filter is integrated with the three-point trapezoidal and Simpson quadrature. The former produces abut 30% greater viscosity in the core flow than the latter.

At the higher Reynolds number 12 500 the channel flow was computed by utilizing one grid size only. The trend in the results was similar to that of the low Reynolds number case. The streamwise fluctuations are overpredicted and the friction is underpredicted. The non-modelled computation oscillates non-physically and the SGS models stabilize the computation and improve the results especially in the core flow where the cell volumes of the stretched gird are large. The simple Smagorinsky model accompanied by the van Driest damping function works best among the applied models. In the dynamic model the numerical implementation affects a lot. The volume over which the eddy viscosity is calculated, becomes relatively large. The resolution that has been applied to the case might be too coarse for the dynamic model. On the other hand, a second-order finite-difference approximation includes a lot of numerical truncation errors as small filtering molecules are applied. A longer filter cuts the subgrid frequencies more sharply but the proper implementation is more tedious and the resolution of the computation should probably be finer.

The discretization error was assessed at $Re_b = 2800$. The estimated error dominates the accurate subgrid term by a factor of ten even if the filter width is twice that of the grid spacing. Only in the vicinity of the walls both terms are about equal in size. A perfect SGS model will not necessarily improve the result in this case. However, a dissipation caused by the eddy viscosity might stabilize the computation and remove unphysical oscillations, as it did at $Re_b = 12\,500$.

Najjar and Tafti [9] concluded that an improved result must not be taken for granted by applying a subgrid-scale model in a finite-difference calculation. If the resolution of the grid is fine enough to provide a physically reasonable solution without any dissipation, the present results support the same conclusion. Studies with higher Reynolds numbers are required to clarify the advantages of the SGS modelling in finite volume solutions.

ACKNOWLEDGEMENTS

This research project has been funded by Academy of Finland and the CODE program of the National Technology Agency TEKES whose support is gratefully acknowledged.

REFERENCES

1. Smagorinsky J. General circulation experiments with the primitive equations. Part I: The basic experiment. *Monthly Weather Review* 1963; **91**:99–152.
2. Deardorff JW. A numerical study of three-dimensional turbulent channel flow at large Reynolds numbers. *Journal of Fluid Mechanics* 1970; **41**:453–480.
3. Moin P, Kim J. Numerical investigation of turbulent channel flow. *Journal of Fluid Mechanics* 1982; **118**: 341–377.
4. Piomelli U, Zang TA, Speziale CG, Hussaini MY. On the large-eddy simulation of transitional wall-bounded flows. *Physics of Fluids A* 1990; **2**(2):257–265.
5. Germano M, Piomelli U, Moin P, Cabot WH. A dynamic subgrid-scale eddy viscosity model. *Physics of Fluids A* 1991; **7**:1760–1765.
6. Lilly DK. A proposed modification of the Germano subgrid-scale closure method. *Physics of Fluids A* 1992; **4**:633–635.
7. Piomelli U. High Reynolds number calculations using the dynamic subgrid-scale stress model. *Physics of Fluids A*, 1993; **5**(7):1484–1495.
8. Balaras E, Benocci C, Piomelli U. Finite-difference computations of high reynolds number flows using the dynamic subgrid-scale model. *Theoretical and Computational Fluid Dynamics* 1995; **7**:207–216.
9. Najjar FM, Tafti DK. Study of discrete test filters and finite difference approximations for the dynamic subgrid-scale stress model. *Physics of Fluids* 1996; **8**(4):1076–1088.
10. Najjar FM, Tafti DK. Evaluation of the dynamic subgrid-scale stress model in finite differenced LES: effects of grid resolution and inhomogeneous test filtering. In *Symposium on LES and DNS of Turbulent Flow*, Atlanta, FED-vol. 242, Nov 1996; pp 229–236.
11. Sagaut P, Montreuil E, Labbé O. Assessment of some self-adaptive SGS models for wall bounded flows. *Aerospace Science and Technology*, 1999; **3**(6):335–344.
12. Burden RL, Faires JD. *Numerical Analysis*, (5th Ed.). PWS Publishing Company; 1993 ISBN 0-534-93219-3.
13. Chorin AJ. Numerical solution of the Navier–Stokes equations. *Mathematics of Computation* 1968; **23**:341–354.
14. Majander P. Developments in Large Eddy Simulation *Licentiate's Thesis*, Helsinki University of Technology, December 1999.
15. Kim J, Moin P, Moser R. Turbulence statistics in fully developed channel flow at low reynolds number. *Journal of Fluid Mechanics* 1987; **177**:133–166.
16. Hussain AKMF, Reynolds WC. Measurements in Fully Developed Turbulent Channel Flow. *Transactions of the ASME* 1975; **97**(12):568–580.
17. Wei T, Willmarth WW. Reynolds-number effects on the structure of a turbulent channel flow. *Journal of Fluid Mechanics* 1989; **204**:57–95.
18. Vreman B, Geurts B, Kuerten H. Discretization error dominance over subgrid terms in large eddy simulation of compressible shear layers in 2D. *Communications in Numerical Methods in Engineering* 1994; **10**:785–790.
19. Vreman B, Geurts B, Kuerten H. *A priori* tests of large eddy simulation of the compressible plane mixing layer. *Journal of Engineering Mathematics* 1995; **29**:299–327.
20. Clark RH, Ferziger JH, Reynolds WC. Evaluation of subgrid-scale models using an accurately simulated turbulent flow. *Journal of Fluid Mechanics* 1979; **91**:1–16.

